Contrib Mineral Petrol (2013) 166:887–910
DOI 10.1007/s00410-013-0899-9

ORIGINAL PAPER

Melts of garnet lherzolite: experiments, models and comparison to melts of pyroxenite and carbonated lherzolite

Timothy L. Grove · Eva S. Holbig · Jay A. Barr · Christy B. Till · Michael J. Krawczynski

Received: 18 September 2012 / Accepted: 28 May 2013 / Published online: 22 August 2013

Abstract Phase equilibrium experiments on a compositionally modified olivine leucitite from the Tibetan plateau have been carried out from 2.2 to 2.8 GPa and 1,380–1,480 °C. The experiments-produced liquids multiply saturated with spinel and garnet lherzolite phase assemblages (olivine, orthopyroxene, clinopyroxene and spinel ± garnet) under nominally anhydrous conditions. These SiO_2-undersaturated liquids and published experimental data are utilized to develop a predictive model for garnet lherzolite melting of compositionally variable mantle under anhydrous conditions over the pressure range of 1.9–6 GPa. The model estimates the major element compositions of garnet-saturated melts for a range of mantle lherzolite compositions and predicts the conditions of the spinel to garnet lherzolite phase transition for natural peridotite compositions at above-solidus temperatures and pressures. We compare our predicted garnet lherzolite melts to those of pyroxenite and carbonated lherzolite and develop criteria for distinguishing among melts of these different source types. We also use the model in conjunction with a published predictive model for plagioclase and spinel lherzolite to characterize the differences in major element composition for melts in the plagioclase, spinel and garnet facies and develop tests to distinguish between melts of these three lherzolite facies based on major elements. The model is applied to understand the source materials and conditions of melting for high-K lavas erupted in the Tibetan plateau, basanite–nephelinite lavas erupted early in the evolution of Kilauea volcano, Hawaii, as well as younger tholeiitic to alkali lavas from Kilauea.

Keywords Garnet lherzolite · Mantle melting · Tibetan Plateau · Kilauea Hawaii · Experimental petrology

Communicated by G. Moore.

Electronic supplementary material The online version of this article (doi:10.1007/s00410-013-0899-9) contains supplementary material, which is available to authorized users.

T. L. Grove (✉) · E. S. Holbig · J. A. Barr
Department of Earth, Atmospheric and Planetary Sciences, Massachusetts Institute of Technology, Cambridge, MA 02139, USA
e-mail: tlgrove@mit.edu

C. B. Till
US Geological Survey, Menlo Park, CA 94025, USA

M. J. Krawczynski
Department of Earth, Environmental and Planetary Sciences, Case Western Reserve University, Cleveland, OH 44106, USA

Introduction

Liquids in equilibrium with a garnet lherzolite phase assemblage (olivine, orthopyroxene, clinopyroxene and garnet) and/or a garnet pyroxenite assemblage are produced when the Earth's mantle melts at depths greater than ~60 km. Compositional characteristics of these melts can provide fundamental information on the conditions (pressure and temperature) and processes of melting. Few existing models constrain the temperature, pressure and composition of melts of garnet lherzolites. Longhi (2002) provided an experimental data set from 2.4 to 3.4 GPa and used his new experiments and literature data (Kinzler 1997; Walter and Presnall 1994) to develop a model for calculating the major element compositions of melts of garnet lherzolite. Gudfinnsson and Presnall (2005) developed discriminant diagrams using CaO, MgO, Al_2O_3 and SiO_2

co-variations to identify compositional trends specific to garnet lherzolite melts. Herzberg and Asimow (2008) provide a model that extends into pressures of garnet lherzolite stability that also utilizes some of the data used by Longhi (2002). These pioneering studies and models have provided a framework for further identifying and studying deep mantle melts, but have been necessarily limited in scope for reasons discussed below.

There are several reasons why so few garnet lherzolite-saturated liquids are reported in the experimental literature. The first concerns direct melting experiments that use lherzolite as a starting material. Clinopyroxene and garnet are exhausted at relatively low extents of melting, and measuring the composition of the liquid at low extents of melting can be extremely challenging (e.g., Baker and Stolper 1994). Secondly, exploring the multiphase saturation regions using high-pressure crystallization experiments on basalts with variable compositions (e.g., Kinzler 1997) is a method that allows for easier analysis of melt compositions. However, the small temperature interval over which liquid and olivine + orthopyroxene + clinopyroxene + garnet coexist (often less than 10 °C) is similar to the temperature reproducibility of the piston cylinder technique. The third reason for the paucity of experimental data is that the high-pressure crystallization liquid lines of decent in basaltic systems follow peritectic saturation boundaries leading to the garnet lherzolite equilibrium. Thus, crystallizing liquids frequently "miss" the garnet lherzolite equilibrium if the mineral in reaction with liquid is exhausted. A fourth and final reason is that the pressure–temperature range of garnet lherzolite stability is near the limit of that accessible with piston cylinder experimental techniques.

This paper addresses these experimental obstacles with new experiments of garnet lherzolite-saturated liquids and uses them along with published experimental data to explore the influence of pressure, temperature and variations in major element source compositions on garnet lherzolite melting. We develop a model for garnet lherzolite melting of compositionally variable (metasomatized, primitive and depleted) mantle that follows the approach of Kinzler and Grove (1992a, b). The experimental results presented here expand the data set of garnet lherzolite melts by ~30 % and include a wider range of bulk compositions. Along with exploring the influence of mantle metasomatism and melt depletion on the compositions of garnet lherzolite facies melts, we provide a technique that uses major element information to discriminate mantle lherzolite melts from melts of pyroxenite and carbonated lherzolite. We apply the model to understand melting processes recorded in alkali lavas from the Tibetan plateau and the range of lava compositions erupted from Kilauea, Hawaii.

Experimental and analytical methods

Starting material

A modified version of the olivine leucitite (BB-107) from the experiments of Holbig and Grove (2008) was used as a starting material for new experiments. BB-107, a high-K, SiO_2-undersaturated composition was strategically chosen to locate high-pressure liquids saturated with olivine (oliv) + orthopyroxene (opx) + high Ca clinopyroxene (cpx) + garnet (gar). The composition of BB-107 was first adjusted for the effects of high-pressure fractional crystallization by the numerical iterative addition of the relevant high-pressure fractionating assemblage in 1 % by weight increments. The high-pressure fractionating assemblage is 0.15 oliv + 0.85 cpx as determined by Holbig and Grove (2008), and the calculation iterations were carried out until the modified BB-107 composition would be in equilibrium with Fo_{90} olivine. This fractionation-adjusted composition was then compared to a garnet-spinel lherzolite-saturated liquid (L69) from Kinzler (1997) with much lower alkali contents and was used to determine a hybrid composition (BBGtOpx) with Mg/(Mg + Fe) major element characteristics of L69 and the high alkali and P_2O_5 contents of the Tibetan olivine leucitite. BBGtOpx was prepared as a starting material by adding natural minerals to create the predicted bulk composition. The bulk composition of BBGtOpx, the basalt (BB-107) and natural minerals used in creating BBGtOpx are reported along with the experimental results (see Tables 1, 2).

Piston cylinder experiments

The melting experiments were carried out from 2.2 to 2.8 GPa and 1,380–1,480 °C in a 0.5-inch solid-medium piston cylinder device (Boyd and England 1960). The pressure medium was $BaCO_3$ and pressure was calibrated using the Ca-Tschermak breakdown reaction (Hays 1967) and the garnet to spinel phase transition in the CMAS-6 bulk composition of Longhi (2005). The temperature was monitored and controlled using a $W_{97}Re_3 - W_{75}Re_{25}$ thermocouple and corrected for a temperature difference of 20 °C between the hotter center of the run assembly and the colder position of the thermocouple that is offset above the center. The temperature was not corrected for the effect of pressure on the thermocouple EMF. The run temperature was maintained by a Eurotherm 818 controller to ±2 °C, and we judge temperature reproducibility to be ±10 °C.

Nominally anhydrous experiments were performed in a graphite capsule machined from dense high-purity Specpure™ graphite rods. The starting material (~0.04 g) + graphite capsule assembly was dried for 12 h at 125 °C,

Table 1 Experimental conditions for BBGtopx

Run#	*P* (GPa)	*T* (°C)	*t* (h)	wt%						Mg#					
				Gl	Cpx	Opx	Ol	Sp	Gt	Gl	Cpx	Opx	Ol	Sp	Gt
C275	2.2	1,440	24	100											
C279	2.2	1,420	24.7	95(2)		1.4(1)	2.5(1.2)	0.7(1)		0.77		0.91	0.91	0.83	
C283	2.2	1,410	22.5	88(4)	4.6(4)	2.5(2)	3.8(2)	1.2(2)		0.73	0.88	0.89	0.89	0.80	
C278	2.2	1,400	21.5	78(3)	22(2)		6(1)	4(1)	−9(4)	0.69	0.86		0.87	0.79	0.81
C273	2.4	1,470	25	100											
C272	2.4	1,440	23	82(4)	7(4)	2(2)	2.1(2)		7(3)	0.72	0.88	0.90	0.88		0.84
C276	2.4	1,420	24	60(10)	16(12)	4(8)			17(8)	0.72	0.89	0.90			0.85
C286	2.4	1,415	9	80(2)	8(1)		4(0)		8(1)	0.71	0.88		0.88		0.83
C282	2.4	1,410	23.8	68(3)	9(3)	2.2(2)	1.8(1.8)		19(2)	0.72	0.88	0.90	0.89		0.83
C271	2.4	1,400	24	49(5)	24(4)		2(1)		23(3)	0.65	0.85		0.85		0.79
C270	2.6	1,480	25	100											
C274	2.6	1,440	28	76(3)	10(3)	2.4(2)			12(2)	0.74	0.88	0.90			0.84
C285	2.6	1,435	9.5	65(2)	17(1)				17(1)	0.69	0.87				0.82
C284	2.6	1,430	24.7	73(7)	10(5)		3(2)		15(4)	0.72	0.88		0.89		0.84
C277	2.6	1,400	28.2	54(3)	23(2)		3(1)		21(2)	0.67	0.86		0.86		0.80
C299	2.8	1,460	23	100.00											
C288	2.8	1,440	23.5	73(5)	6(3)				18(3)	0.72	0.88				0.71

Run#	*P* (GPa)	*T* (°C)	*t* (h)	KD[a]					Fe loss[b]	ssr
				Cpx	Opx	Ol	Sp	Gt		
C275	2.2	1,440	24							
C279	2.2	1,420	24.7		0.33	0.33	0.68		−5	0.08
C283	2.2	1,410	22.5	0.36	0.32	0.33	0.66		−1.2	0.02
C278	2.2	1,400	21.5	0.36		0.33	0.60	0.51	−0.30	0.40
C273	2.4	1,470	25							
C272	2.4	1,440	23	0.34	0.29	0.33		0.49	4.5	0.04
C276	2.4	1,420	24	0.32	0.29			0.46	−2.6	5.10
C286	2.4	1,415	9	0.35		0.32		0.52	−0.79	0.59
C282	2.4	1,410	23.8	0.35	0.30	0.31		0.53	4.50	0.04
C271	2.4	1,400	24	0.33		0.32		0.49	−1.6	2.20
C270	2.6	1,480	25							
C274	2.6	1,440	28	0.38	0.31			0.55	−5	0.09
C285	2.6	1,435	9.5	0.33				0.49	−3.3	0.34
C284	2.6	1,430	24.7	0.34		0.34		0.51	−10	2.2
C277	2.6	1,400	28.2	0.32		0.32		0.50	−5.5	0.97
C299	2.8	1,460	23							
C288	2.8	1,440	23.5	0.36			0.59		1.0	0.38

See Table 2 for abbreviations. Runs C279, C283, C272, C282 and C274 used LIME technique of Krawczynski and Olive (2011)

ssr sum of squares of the residual

[a] KD = (XFextl*XMgliq)/(XMgxtl*XFeliq)

[b] Apparent loss or gain of FeO estimated as 100*(FeOcalc − FeOstarting material)/FeOstarting material

placed in a Pt capsule and welded shut. This capsule assembly was surrounded by an Al_2O_3 ceramic cylinder and centered in the hot spot of a graphite heater, using MgO spacers. The furnace assembly design was similar to that used by Hesse and Grove (2003), but the graphite capsule was modified. A capsule with thicker walls and a smaller interior volume ~1-mm-diameter hole and 1 mm in length was utilized. The thicker walls reduced cracking of the capsule, which leads to Fe loss when the melt comes into contact with the outer Pt jacket.

Table 2 Compositions of mineral and liquid phases in BBGtopx experiments

P (kbar)	*T* (°C)	Run #	ϕ	*N*	SiO_2	TiO_2	Al_2O_3	Cr_2O_3	FeO	MnO
22	1,420	C279	gl	12	46.6(1)	0.86(4)	15.6(0)	0.21(2)	7.16(14)	0.19(2)
			opx	19	54.0(5)	0.09(2)	6.22(72)	0.93(10)	5.36(14)	0.16(3)
			ol	9	41.0(1)	0.01(1)	0.14(3)	0.14(2)	8.61(12)	0.16(2)
			sp	7	0.42(4)	0.16(2)	52.9(6)	16.4(6)	7.84(1)	0.16(3)
22	1,410	C283	gl	20	45.7(2)	0.92(8)	15.7(1)	0.11(2)	8.21(19)	0.18(2)
			cpx	19	52.1(1)	0.20(2)	7.74(39)	0.93(8)	4.97(25)	0.18(3)
			opx	24	53.6(6)	0.12(2)	7.21(59)	0.79(5)	6.36(12)	0.16(3)
			ol	7	40.5(4)	0.02(1)	0.11(3)	0.13(2)	10.6(1)	0.19(2)
			sp	6	0.31(4)	0.17(1)	56.2(2)	14.0(6)	9.04(18)	0.13(1)
22	1,400	C278	gl	10	46.3(4)	1.01(6)	16.3(1)	0.10(2)	8.98(8)	0.19(3)
			cpx	18	51.2(5)	0.31(7)	8.40(44)	0.61(15)	5.79(73)	0.18(4)
			ol	11	40.0(5)	0.01(2)	0.14(2)	0.08(3)	12.5(2)	0.18(2)
			gt	7	41.9(3)	0.34(2)	23.3(2)	0.92(6)	7.94(9)	0.29(4)
			sp	8	0.40(5)	0.17(2)	59.4(4)	9.53(14)	10.1(2)	0.11(2)
24	1,440	C272	gl	11	47.7(4)	0.94(7)	15.3(4)	0.12(2)	8.75(37)	0.17(2)
			cpx	18	52.6(3)	0.20(3)	7.33(29)	0.84(11)	5.19(30)	0.18(2)
			opx	17	54.1(3)	0.11(2)	6.63(45)	0.72(5)	6.29(9)	0.16(3)
			gt	8	42.3(2)	0.30(4)	23.4(2)	1.46(13)	6.74(11)	0.28(2)
			ol	9	40.5(3)	0.03(1)	0.15(4)	0.11(1)	11.2(2)	0.13(2)
24	1,420	C276	gl	13	47.6(3)	0.89(8)	15.7(3)	0.09(4)	7.29(27)	0.16(4)
			cpx	10	52.1(4)	0.22(2)	7.54(44)	0.54(35)	4.60(26)	0.18(2)
			opx	19	53.5(5)	0.12(2)	7.19(42)	0.71(13)	6.10(17)	0.16(3)
			gt	10	42.2(1)	0.32(3)	23.3(1)	1.39(6)	6.32(10)	0.28(2)
24	1,415	C286	gl	15	45.6(5)	0.96(6)	15.1(2)	0.11(3)	8.94(30)	0.17(2)
			cpx	22	52.3(4)	0.25(2)	7.65(24)	0.90(9)	5.04(23)	0.17(3)
			ol	9	40.5(3)	0.03(1)	0.15(4)	0.11(1)	11.2(2)	0.13(2)
			gt	12	42.3(2)	0.25(1)	23.6(2)	1.22(22)	7.58(44)	0.30(3)
24	1,410	C282	gl	10	45.3(2)	1.18(7)	15.9(1)	0.09(2)	8.00(9)	0.16(2)
			cpx	21	52.2(4)	0.27(4)	7.71(32)	0.62(5)	4.82(23)	0.16(2)
			opx	8	53.1(2.0)	0.12(3)	4.80(51)	0.37(5)	6.96(41)	0.13(2)
			ol	5	40.3(1)	–	0.21(8)	0.07(1)	10.3(2)	0.18(1)
			gt	9	41.9(2)	0.28(6)	23.5(1)	1.01(10)	7.38(34)	0.29(4)
24	1,400	C271	gl	12	47.0(2)	1.23(6)	15.1(1)	0.07(2)	9.84(20)	0.17(3)
			cpx	17	52.6(4)	0.30(3)	7.26(32)	0.51(3)	6.15(18)	0.17(2)
			ol	6	39.9(4)	0.01(1)	0.14(1)	0.06(2)	14.0(2)	0.19(2)
			gt	7	41.7(4)	0.44(14)	23.5(1)	0.85(7)	8.46(24)	0.29(2)
26	1,440	C274	gl	18	46.4(4)	0.94(9)	14.7(4)	0.11(4)	8.23(37)	0.15(3)
			cpx	18	53.3(4)	0.20(1)	6.82(32)	0.63(3)	4.99(17)	0.18(2)
			opx	14	55.1(3)	0.10(2)	4.86(14)	0.35(3)	6.32(9)	0.14(2)
			gt	11	41.9(3)	0.31(4)	23.5(2)	1.22(8)	7.03(38)	0.27(3)
26	1,435	C285	gl	23	45.3(3)	1.06(8)	14.5(3)	0.07(2)	9.46(22)	0.18(2)
			cpx	20	52.4(3)	0.27(5)	7.28(27)	0.58(9)	5.08(26)	0.16(2)
			gt	15	42.3(1)	0.21(6)	23.9(2)	0.98(6)	7.81(38)	0.30(4)
26	1,430	C284	gl	10	45.2(2)	1.11(7)	14.3(2)	0.12(2)	8.08(19)	0.18(3)
			cpx	19	52.8(3)	0.23(2)	7.23(30)	0.62(7)	4.83(24)	0.17(3)
			ol	6	41.0(3)	0.02(1)	0.26(11)	0.10(2)	10.6(1)	0.11(2)
			gt	9	42.0(2)	0.31(5)	23.5(2)	1.14(9)	7.15(36)	0.25(2)
26	1,400	C277	gl	12	45.3(2)	1.31(7)	14.9(1)	0.05(1)	9.35(1)	0.18(2)
			cpx	18	51.7(4)	0.35(5)	8.05(92)	0.42(12)	5.13(38)	0.14(2)

Table 2 continued

P (kbar)	*T* (°C)	Run #	ϕ	*N*	SiO_2	TiO_2	Al_2O_3	Cr_2O_3	FeO	MnO
			ol	6	40.3(4)	–	0.15(4)	0.06(1)	13.0(3)	0.18(2)
			gt	7	42.1(5)	0.44(7)	23.8(2)	0.59(15)	7.99(19)	0.29(1)
28	1,440	C288	qgl	38	46.3(1.4)	1.28(16)	13.9(1.6)	0.06(6)	9.03(67)	0.18(3)
			cpx	10	52.4(4)	0.28(5)	7.36(49)	0.49(6)	4.75(7)	0.14(1)
			gt	7	41.7(4)	0.17(10)	23.6(1)	0.95(13)	8.09(37)	0.33(2)
BBGtopx					44.57	0.85	14.76	0.33	8.42	0.2
BB107					45.47	1.26	12.56	0	9.03	0.16
garnet					42.4	0.16	23.7	1.06	8.14	0.31
opx					56.1	0.15	3.4	0.42	6.32	0.11

P (kbar)	*T* (°C)	Run #	ϕ	*N*	MgO	CaO	Na_2O	K_2O	P_2O_5	Total
22	1,420	C279	gl	12	13.7(1)	9.40(9)	2.28(15)	2.11(5)	0.73(7)	98.9
			opx	19	31.4(3)	2.19(6)	0.16(3)			100.4
			ol	9	50.3(5)	0.27(1)	–			100.6
			sp	7	22.0(1)	0.13(1)				100.0
22	1,410	C283	gl	20	12.5(1)	9.10(8)	2.42(14)	2.48(3)	1.01(5)	98.3
			cpx	19	21.1(6)	12.6(6)	0.73(4)			100.5
			opx	24	30.2(3)	2.14(12)	0.15(3)			100.8
			ol	7	48.1(3)	0.29(5)				99.9
			sp	6	20.9(6)	0.07(2)	0.01(1)	0.05(4)		100.8
22	1,400	C278	gl	10	11.2(2)	8.35(10)	2.77(14)	2.78(8)	0.97(8)	99.0
			cpx	18	20.0(9)	13.0(1.5)	0.84(14)			100.3
			ol	11	47.7(2)	0.28(2)				100.9
			gt	7	19.5(5)	5.93(11)	0.02(1)			100.1
			sp	8	20.9(2)	0.12(2)				100.8
24	1,440	C272	gl	11	12.4(6)	9.03(5)	2.47(27)	2.16(52)	0.96(8)	100.1
			cpx	18	21.9(6)	11.6(8)	0.77(5)			100.6
			opx	17	30.5(2)	2.18(7)	0.17(3)			100.9
			gt	8	19.4(2)	5.40(2)	0.01(1)			99.2
			ol	9	47.7(4)	0.36(9)				100.2
24	1,420	C276	gl	13	10.6(8)	8.43(72)	2.66(31)	3.24(73)	1.14(8)	97.8
			cpx	10	20.9(5)	12.9(9)	0.91(5)			99.9
			opx	19	30.5(4)	2.11(10)	0.19(3)			100.5
			gt	10	20.0(8)	5.92(1)	–			99.7
24	1,415	C286	gl	15	12.4(4)	8.93(4)	2.70(30)	2.64(34)	1.22(15)	98.8
			cpx	22	20.0(5)	13.8(7)	0.90(5)			101.1
			ol	9	47.7(4)	0.36(9)				100.2
			gt	12	20.3(3)	5.45(63)	–			101.0
24	1,410	C282	gl	10	11.64(20)	8.14(12)	3.42(38)	3.40(8)	1.36(10)	97.3
			cpx	21	20.0(4)	13.8(6)	1.01(1)			100.6
			opx	8	33.6(1.9)	1.14(16)	0.14(1)			100.4
			ol	5	48.4(2)	0.38(6)	0.01(1)			99.9
			gt	9	20.1(3)	5.53(23)	0.04(1)			100.0
24	1,400	C271	gl	12	10.3(1)	7.56(8)	3.19(14)	3.78(4)	1.52(1)	99.7
			cpx	17	19.4(3)	13.3(4)	1.04(5)	–	–	100.7
			ol	6	45.9(9)	0.28(2)	0.02(2)	–	–	100.6
			gt	7	18.0(3)	5.80(39)	0.03(1)	–	–	99.0
26	1,440	C274	gl	18	11.6(1.27)	8.25(90)	2.91(49)	3.21(83)	1.26(11)	97.9
			cpx	18	21.2(4)	12.6(4)	0.96(4)			100.9

Table 2 continued

P (kbar)	*T* (°C)	Run #	ϕ	*N*	MgO	CaO	Na_2O	K_2O	P_2O_5	Total
			opx	14	32.5(3)	0.88(11)	0.09(2)			100.4
			gt	11	20.2(7)	5.47(17)	0.02(2)			99.9
26	1,435	C285	gl	23	12.1(8)	8.34(68)	2.91(33)	3.33(78)	1.28(7)	98.5
			cpx	20	19.5(7)	14.3(7)	1.09(11)			100.7
			gt	15	20.2(2)	5.22(37)	–			100.9
26	1,430	C284	gl	10	11.7(3)	8.39(7)	3.82(55)	2.93(20)	1.22(7)	97.1
			cpx	19	20.4(5)	13.6(7)	0.96(8)			100.8
			ol	6	47.5(5)	0.51(11)				100.1
			gt	9	20.4(3)	5.68(24)	–			100.4
26	1,400	C277	gl	12	10.7(3)	7.58(8)	4.10(23)	4.12(10)	1.65(9)	99.3
			cpx	18	18.4(4)	14.5(7)	1.30(14)			100.0
			ol	6	46.2(4)	0.32(8)	–			100.2
			gt	7	18.2(1)	6.02(18)	0.04(1)			99.4
28	1,440	C288	qgl	38	13.2(1.8)	9.7(1.2)	2.47(65)	2.1(1.1)	1.25(19)	99.4
			cpx	10	19.3(3)	14.7(3)	1.31(3)			100.7
			gt	7	19.9(4)	5.35(54)	0.07(4)			100.1
BBGtopx					14.85	9.07	2.12	2.48	0.97	100
BB107					10.43	12.25	3.35	3.94	1.55	
garnet					20.7	4.74	0	0	0	
opx					33.9	0.66	0.14	0	0	

Each analysis shows one standard deviation of the average of replicate analyses in terms of least units cited. Thus, 46.6(1) should be read 46.6 ± 0.1

gl glass, *opx* orthopyroxene, *ol* olivine, *sp* spinel, *cpx* clinopyroxene, *gt* garnet, *qgl* glass + quench crystals, *N* number of analyses

Experimental assemblies were first pressurized to 1.0 GPa at room temperature conditions. This pressure was maintained while the sample was heated at a rate of 100 °C/min to 865 °C and held at this temperature for 6 min. After 3 min at 865 °C, the pressure was raised to the final run pressure. The temperature was then increased by 50 °C/min to the run temperature and the pressure was frequently monitored and adjusted to the desired final experimental pressure. The pressure was held constant using the piston-in technique (Johannes et al. 1971). After ~24–28 h, the experiments were quenched by turning off the output power. The oxygen fugacity of our experiments has not been measured directly. Médard et al. (2008) have measured conditions of 1–2 log units below the quartz–fayalite–magnetite buffer for the piston cylinder assemblies used in our laboratory.

Electron microprobe analysis

All quenched experiments were cut in half, mounted in epoxy and polished. The samples were then carbon coated and analyzed on the MIT JEOL-JXA-733 Superprobe, using wavelength-dispersive spectrometry with a 10 nA beam current and an accelerating voltage of 15 kV. For glass analyses, the beam diameter was set to ~10 μm, and Na was counted at the beginning of the analysis for 5 s. Other elements were measured for up to 40 s, depending on abundance level. Analytical precision can be inferred from replicate analyses of glass working standards (Gaetani and Grove 1998). One standard deviation of the average of replicate glass analyses for each oxide expressed as relative percent of oxides is $SiO_2 = 0.4$ %, $Al_2O_3 = 0.9$ %, CaO = 1.5 %, MgO = 1.5 %, FeO = 1.4 %, MnO = 8.1 %, $P_2O_5 = 5$ %, $Na_2O = 1.9$ %, and $K_2O = 1.1$ % based on 289 individual measurements over 28 analytical sessions. The CITZAF correction package of Armstrong (1995) was used to reduce the data and to obtain quantitative analysis. The atomic number correction of Duncumb and Reed, Heinrich's tabulation of absorption coefficients, and the fluorescence correction of Reed were used to obtain a quantitative analysis as outlined in Armstrong (1995).

Experimental results

Experiments with the hybrid starting material (BBGtOpx) were conducted at 2.2–2.8 GPa and 1,380–1,480 °C (Fig. 1). The conditions for these experiments are presented in Table 1 and compositions of the experimental products are found in Table 2. Two of the experiments at 2.4 GPa show simultaneous saturation of the melt with

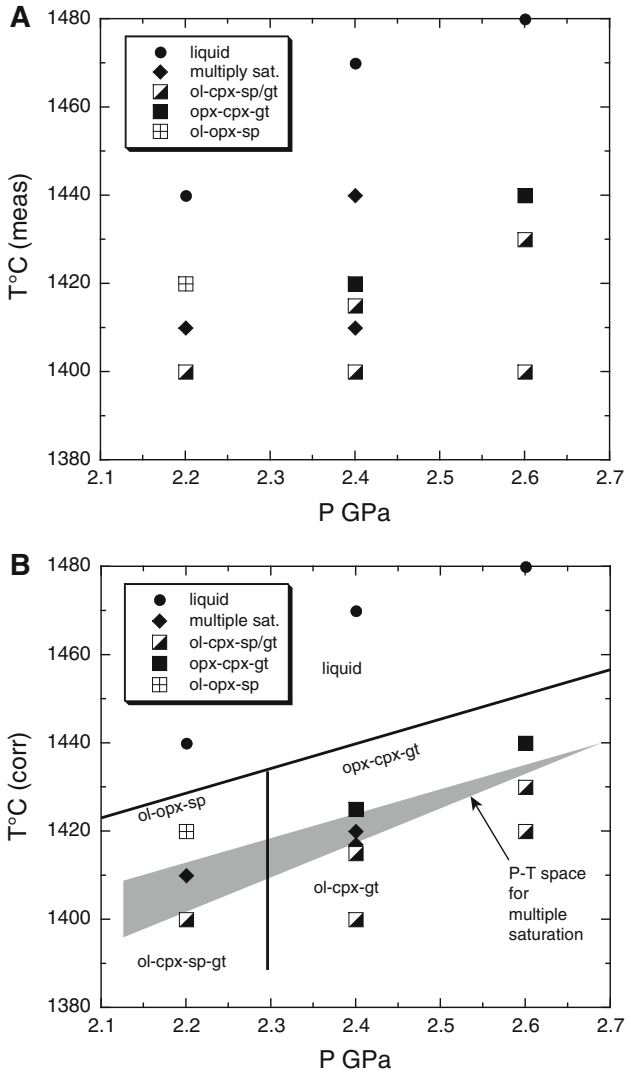

Fig. 1 Pressure–temperature conditions of experiments on the BBG-tOpx compositions. **a** Uncorrected experimental results. **b** Temperature-corrected data using the 2.2 GPa experimental results and liquid Mg# in the 2.4 and 2.6 GPa experiments. Adjusting temperature of the 2.4 and 2.6 experiments results in the expected phase appearance sequence (see text and Fig. 3). A field for the garnet lherzolite-saturated liquids is shown in gray

olivine (oliv), orthopyroxene (opx), clinopyroxene (cpx) and garnet (gar) and in one experiment, at 2.2 GPa, spinel is present with liquid + oliv + opx + cpx. Figure 2 shows a back-scattered electron image of one of the multiply saturated experiments; sample C282 (2.4 GPa, 1,410 °C), in which the melt is saturated with the complete garnet lherzolite assemblage (oliv + opx + cpx + gar).

The phase diagram for the BBGtOpx starting material is shown in Fig. 1a. Melt is saturated with a garnet lherzolite assemblage over the interval of 1,400–1,415 °C at 2.2 GPa and at ~1,430 °C at 2.6 GPa. Melt is saturated with a spinel lherzolite assemblage (oliv + opx + cpx + spinel) at 1,410 °C at 2.2 GPa. The temperature range over which

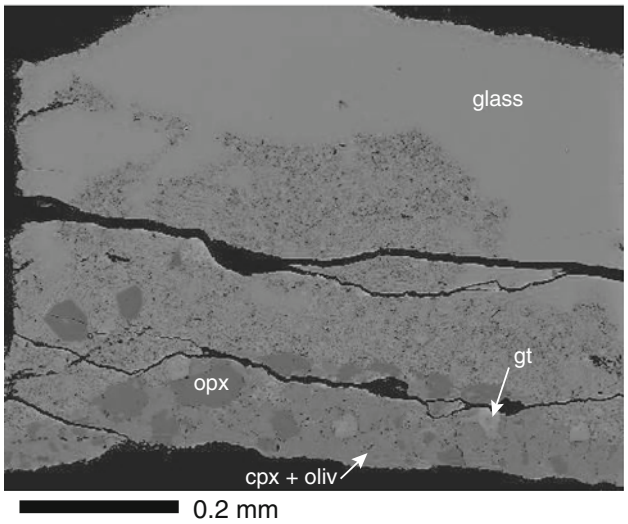

Fig. 2 Experimental run product multiply saturated with a garnet lherzolite assemblage (oliv + opx + cpx + gar). Crystalline phases and glass segregate in the small temperature gradient (<7 °C) across the capsule. Melt is quenched to a glass at the upper hot end of the capsule, and a region of quench crystals grew during quenching in the vicinity of the minerals at the colder end of the capsule. *Dark outer margin* is the graphite capsule and *dark lines across the capsule* are epoxy-filled cracks

the experimental melts are saturated with a garnet lherzolite assemblage shrinks as pressure increases. At 2.8 GPa, cpx + gar are present at 1,440 °C (C288, Tables 1, 2) and the liquidus is located between 1,440 and 1,460 °C (C299). At 2.8 GPa, crystallization of cpx + gar move the residual liquids away from the garnet lherzolite multiple saturation equilibrium. In this study, it was necessary to place experiments at temperature intervals of 5–10 °C, an interval that is close to or below our reproducibility of 10 °C, in order to cover the short temperature interval over which the five-phase equilibrium occurs and to locate the key phase boundaries. The phase appearance sequence with decreasing temperature in the 2.2 GPa experiments (Fig. 1) changes from oliv + opx + sp to oliv + opx + cpx + sp and finally to oliv + cpx + sp. This is the expected change in phase appearance as a melt passes through the four-phase equilibrium saturation with oliv + opx + cpx + sp at pressures above ~2 GPa (Kinzler 1997). The mineral and melt compositions also change in a systematic manner. This is illustrated in Fig. 3 where liquid Mg# is plotted versus temperature and follows a linear trend. The 2.4 and 2.6 GPa experiments do not show the same phase appearance sequence and systematic changes with decreasing temperature. Therefore, we used the variations in the 2.2 GPa liquid compositions with temperature to estimate more precisely the temperatures of the 2.4 and 2.6 GPa experiments. This was accomplished by fitting a line by visual inspection to the 2.2 GPa experiments and then

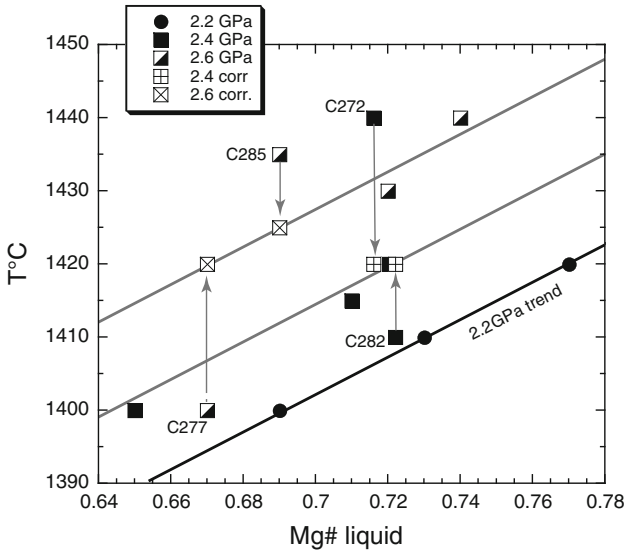

Fig. 3 Measured Mg# of glasses in the BBGtOpx experiments. The 2.2 GPa trend of Mg# versus temperature was used to correct the temperature of the 2.4 and 2.6 GPa experiments

fitting a line of the same slope to three of the 2.4 GPa experiments and two of the 2.6 GPa experiments (Fig. 3). These two lines were chosen a priori to be equally spaced in temperature since the experiments were equally spaced in pressure and with slopes parallel to that defined by the 2.2 GPa experiments (C278, C279 and C283). The two lines were used to adjust the accepted temperatures of the remaining 2.4 and 2.6 GPa experiments. When the corrected temperatures are used for these 2.4 and 2.6 GPa experiments, the phase diagram (Fig. 1b) illustrates the appropriate change in phase assemblage with temperature. At 2.4 and 2.6 GPa, there is a high-temperature mineral assemblage of opx + cpx + gar followed by a multiple saturation field of oliv + opx + cpx + gar. On the low temperature side of the multiple saturation field, the mineral assemblage is oliv + cpx + gar.

The mineral phases in all the experiments are compacted at the bottom of the capsule (Fig. 2); a phenomenon that we assume is caused by chemical diffusion and relative migration of phases due to a thermal gradient (Walker and Agee 1988). The hot spot of the assembly used lies on the uppermost part of the capsule; the bottom of the capsule is ~7 °C colder (Médard et al. 2008).

Mass balance and approach to equilibrium

For each experiment, we used a mass balance technique to estimate phase proportions and to determine whether the bulk composition of the experimental sample had remained constant. A linear regression of the compositions of the phases analyzed in each experiment and the bulk composition of the starting material provided estimates of phase proportions. For experiments containing oliv and opx, linear regression commonly yields negative coefficients for one of these two phases. Therefore, we used the regression technique of Krawczynski and Olive (2011) to estimate phase proportions for those experiments. The comparison of the experiment's bulk composition to the bulk composition of the starting material suggests there was no significant loss or gain (<5 %) of any element (Table 1). It is not possible to definitively prove that experiments achieved chemical equilibrium. This would require reversal experiments for all possible compositional changes in all phases. However, for the reasons outlined below, we conclude that the experiments approached equilibrium sufficiently to allow us to understand the crystallization behavior at multiple phase saturation. Although the phase appearances have not been reversed, it has been demonstrated that direct synthesis is sufficient to recover equilibrium phase appearance temperatures in experiments with >40 wt% melt (Grove and Bence 1977). Furthermore, we maintained constant sample composition with generally less than 5 % relative gain of FeO in the bulk sample (Table 1), an important prerequisite for an approach to equilibrium. We also achieved regular and consistent partitioning of major elements between crystalline phases and melt, an additional prerequisite for approaching equilibrium (Table 1). The compositions of opx and gar that grew during the experiments (Table 2) are all substantially different than the compositions of the natural minerals (also reported in Table 2, bottom) that were added to adjust the BBGtOpx composition.

The 17 experiments reported here vary from above the liquidus to experimental products containing more than 49 wt% melt (Table 1). Glass in each experiment is homogenous judging from the small standard deviations of replicate analyses of glass (Table 2). The Ca, Al and Ti contents of clinopyroxenes in our experiments are comparable to those from longer-duration multiple saturation experiments using basaltic compositions (Gaetani and Grove 1998; Kinzler 1997). The Fe–Mg distribution coefficients K_{DFe-Mg} (where $K_{DFe-Mg} = [X^{xtl}_{Fe} * X^{liq}_{Mg}]/[X^{xtl}_{Mg} * X^{liq}_{Fe}]$) are close to constant in these experiments (Table 1). The mean Fe–Mg partition coefficient K_{DFe-Mg} between olivine and melt is 0.32 (±0.01). The K_{DFe-Mg}(cpx–liq) for clinopyroxene is 0.34 (±0.02). The K_{DFe-Mg}(opx − liq) for orthopyroxene is 0.31 (±0.02). The K_{DFe-Mg}(garnet − liq) and K_{DFe-Mg}(spinel − liq) are 0.51 (±0.02) and 0.65 (±0.04), respectively, similar to values reported by Kinzler (1997). At these high temperatures (>1,400 °C) with large amounts of melt present, the consistent partitioning and minor element composition of solid phases observed in our experiments indicate that the experimental phases are close enough to equilibrium to aid in the understanding garnet lherzolite melting.

Discussion

Locating garnet lherzolite-saturated liquids

The experiments carried out in this study, when combined with published experimental data allow us to determine the pressure–temperature conditions under which liquid is saturated with a garnet lherzolite assemblage (oliv + opx + cpx + gar) and the conditions of the spinel to garnet lherzolite transition. The nature of the melting reaction at the high-pressure limit of spinel stability and in the garnet stability field has been characterized in several studies (Kinzler 1997; Kinzler and Grove 1999; Longhi 1995, 2002) and is a peritectic:

$$\text{Olivine} + \text{Clinopyroxene} + \text{Garnet}\ (\text{or Spinel}) = \text{Orthopyroxene} + \text{Liquid} \quad (1)$$

During down-temperature crystallization of basalt in equilibrium with a garnet lherzolite assemblage, the liquid composition remains saturated with all the solid phases at this multiple saturation point (MSP) in composition space, until either orthopyroxene (opx) or liquid is consumed. When opx is exhausted, the melt leaves the MSP and moves along the oliv + cpx + spinel/gar boundary. This behavior has been replicated in several experimental studies of garnet/spinel lherzolite melting. Walter (1998) located liquids saturated with oliv + opx + cpx + gar at 4 and 6 GPa (see Walter 1998; Fig. 2) and found a low temperature assemblage at both of these pressures (oliv + cpx + gar) similar to the one in our study. Longhi (2002) published experiments from 2.4 to 3.4 GPa and used the existing literature data (Kinzler 1997; Walter and Presnall 1994) to develop a model for melting of garnet lherzolite. Barr and Grove (2013) and this present study have generated 7 additional garnet lherzolite-saturated assemblages. This doubles the number of experiments reported since Longhi (2002) and brings the total number of experimental determination of garnet lherzolite-saturated experimental liquids to 29.

As outlined above, there are two *main* reasons why so few garnet lherzolite-saturated liquids are reported in the literature. The first is the short temperature interval over which the assemblage oliv + opx + cpx + gar + liquid is stable in a single bulk composition, often less than 10 °C, which is smaller than the temperature reproducibility of the piston cylinder technique. This leads to the situation where a reported liquid composition is actually the average of two experiments that bracket the MSP, as is the case for two of the three liquid compositions reported in Longhi (2002) and one liquid reported in this study. The second reason is that the MSP is peritectic and the three- and four-phase saturation boundaries leading to the MSP (oliv + opx + cpx and oliv + opx + gar) are peritectic (subtraction)

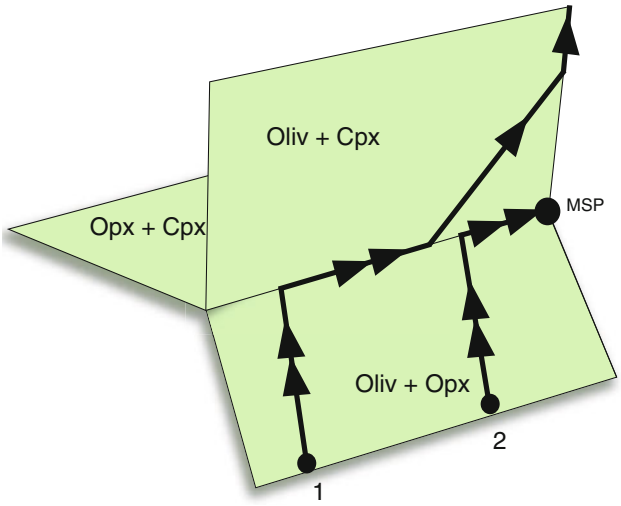

Fig. 4 Schematic three-dimensional representation of the five-phase saturation point (MSP) and four-phase boundary curves and three-phase surfaces in n-dimensional composition space. The oliv + opx + cpx boundary is a reaction boundary and slight changes in bulk composition change the path followed during crystallization. *Lines* depict crystallization paths. *Single arrows* indicate subtraction paths and double arrows indicate reaction paths. Opx reacts out in bulk composition 1 and the crystallization path misses the MSP. For bulk composition 2, opx remains and the crystallization path reaches the MSP

boundaries (Longhi 2002; Barr and Grove 2013). To achieve saturation with the garnet lherzolite assemblage Barr and Grove (2013) adjusted the composition of their starting material as illustrated schematically in Fig. 4. Crystallization experiments will only reach the MSP with decreasing temperature if the bulk composition of the starting material contains enough of the reacting phase so that oliv and/or opx are not consumed while the liquid is on the oliv + opx + cpx boundary. If a phase is consumed, the liquid leaves the three-phase boundary and "misses" the MSP. Both of these reasons contribute to the difficulty of locating the garnet lherzolite MSP. The small temperature interval over which liquid is saturated with the garnet lherzolite assemblage is a distinctive characteristic of garnet lherzolite melts and such behavior has not been observed in natural compositions in equilibrium with plagioclase and spinel lherzolite assemblages (Kinzler and Grove 1992a, b; Kinzler 1997; Till et al. 2012).

Another consequence of the peritectic nature of the oliv + opx + cpx boundary and the oliv + opx + cpx + gar MSP is that the presence of opx on the solidus depends on the bulk composition of the lherzolite. Takahashi (1986) and Walter (1998) found that opx was not on the solidus of their lherzolite melting experiments in the pressure range of >3–7 GPa. This is because the composition of the MSP liquid and cpx vary with pressure and temperature, with cpx becoming less Ca-rich and thus more abundant on a

modal basis as pressure and temperature increase. Therefore, two different types of melting and crystallization sequences are possible depending on pressure and the lherzolite bulk composition as discussed by Longhi (2002; see his Fig. 11). If the bulk composition plots within the oliv − opx − cpx − gar four-phase region, the first melt will be saturated with oliv + opx + cpx + gar, but if the lherzolite bulk composition plots outside of the oliv + opx + cpx + gar four-phase region, the first melt will be saturated with oliv + cpx + gar. This observation implies that near solidus melts of a range of lherzolite compositions produced at certain P–T conditions (>3 GPa) could be difficult to differentiate from pyroxenite melts, because the only pyroxene in the residue is cpx.

Melting systematics of the BBGtOpx composition

In the BBGtOpx composition studied here, the down-temperature change in phase appearance at each pressure illustrates what would be expected as the multiple saturation boundary moves through composition space with increasing pressure. The composition of a melt in equilibrium with a mantle lherzolite becomes more olivine-rich with increasing pressure (Presnall et al. 1979) and the two- and three-phase boundaries associated with the four-phase multiple saturation move through composition space in the manner illustrated in Fig. 5 (schematically shown projected into pseudo-ternary space). At a pressure of 2.2 GPa, the BBGtOpx composition initially crystallizes oliv + opx + sp. With decreasing temperature (Fig. 1b), the liquid reaches the four-phase multiple saturation boundary with oliv + opx + cpx + sp. The liquid remains saturated with all four solid phases until orthopyroxene (opx) is consumed. The melt then moves down the oliv + cpx + sp + gar boundary (Figs. 1b, 5). As pressure increases to 2.4 GPa, the multiple saturation boundary has moved to more olivine-normative compositions, resulting in a change in the liquidus phase assemblage with opx + cpx + gar crystallizing first. As temperature decreases (Fig. 1b), the melt becomes saturated with oliv + opx + cpx + gar and opx + liquid react. When opx is consumed, the melt moves away from the multiple saturation boundary along the oliv + cpx + gar boundary (Fig. 5).

Garnet lherzolite melting model

The garnet lherzolite-saturated liquids produced in this study were combined with other experimentally produced garnet lherzolite equilibria to develop a model for peridotite melting in the garnet stability field. A survey of the literature revealed six other studies where liquids were in equilibrium with oliv + opx + cpx + gar. Experiments from Walter and Presnall (1994), Gudfinnsson and Presnall (1996), Kinzler (1997), Walter (1998), Longhi (2002) and Barr and Grove (2013) (Table 3) report both liquid and solid phase compositions and provide a data set of 29 experiments. Two additional studies that produced garnet lherzolite-saturated liquids (Takahashi 1986; Kushiro 1996) were excluded from the model because the inclusion of data from these studies introduced significant scatter and diminished the quality of the model fits. These two sets of experiments used lherzolitic starting materials similar to Walter (1998), so there is no reason to expect them to deviate. We suspect that there are experimental and/or analytical differences between the laboratories where the two studies were performed and the laboratories where the

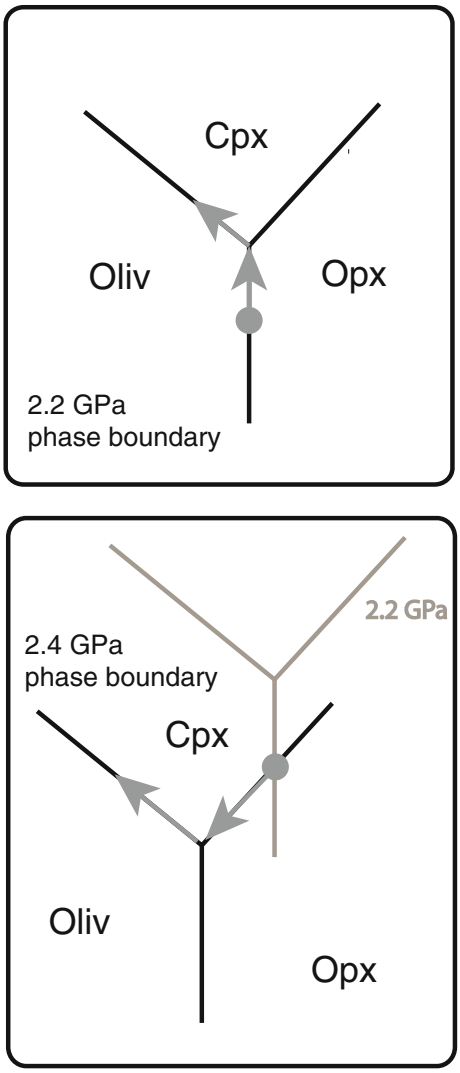

Fig. 5 Schematic representation of the phase relations in the vicinity of the MSP for the BBGtOpx composition (*gray circle*). The MSP with garnet is represented by the intersection of three saturation boundaries: oliv + opx + spinel, opx + cpx + gar and cpx + oliv + gar. Path followed by liquid is shown at 2.2 and 2.4 GPa as phase boundaries move with changing pressure

Table 3 Experiments used in garnet lherzolite melting model

Data source	Expt.#	*P* (GPa)	*T* (°C)	NaK#	Mg#
This study	C283-C278	2.2	1,405	0.350	0.710
	C272	2.4	1,440	0.339	0.720
	C282	2.4	1,410	0.456	0.710
	C274–C284	2.6	1,435	0.384	0.731
Kinzler (1997)	L69	1.9	1,416	0.169	0.740
	L92	1.9	1,396	0.206	0.794
	L82	2.1	1,415	0.236	0.726
	L56	2.1	1,440	0.112	0.762
	L58	2.1	1,430	0.163	0.667
Walter (1998)	40.07	4.0	1,610	0.156	0.769
	60.05	6.0	1,755	0.145	0.820
Gudfinnsson and Presnall (1996)	3,403.11	3.4	1,580	0.161	1.000
	3,503.11	3.5	1,594	0.199	1.000
Longhi (2002)	M1295	2.4	1,480	0.568	0.685
	rD289	2.8	1,577	0.178	0.778
	TM295	2.8	1,530	0.354	0.679
	MO695	2.8	1,510	0.498	0.695
	RD1099-2	2.8	1,567	0.147	0.772
	RD1099-3	2.4	1,520	0.168	0.725
	RD1097-7	3.4	1,635	0.203	0.763
Barr and Grove (2013)	C434	2.35	1,420	0.082	0.510
	C435	2.35	1,440	0.047	0.520
	C436	2.6	1,460	0.031	0.480
Walter and Presnall (1994)	562-1	3.0	1,575	0.000	1.000
	32.62	3.2	1,595	0.000	1.000
	34.63	3.4	1,615	0.000	1.000
	D&S	4.0	1,675	0.000	1.000
	562-1	3.0	1,575	0.000	1.000
	3,402-11	3.4	1,585	0.092	1.000

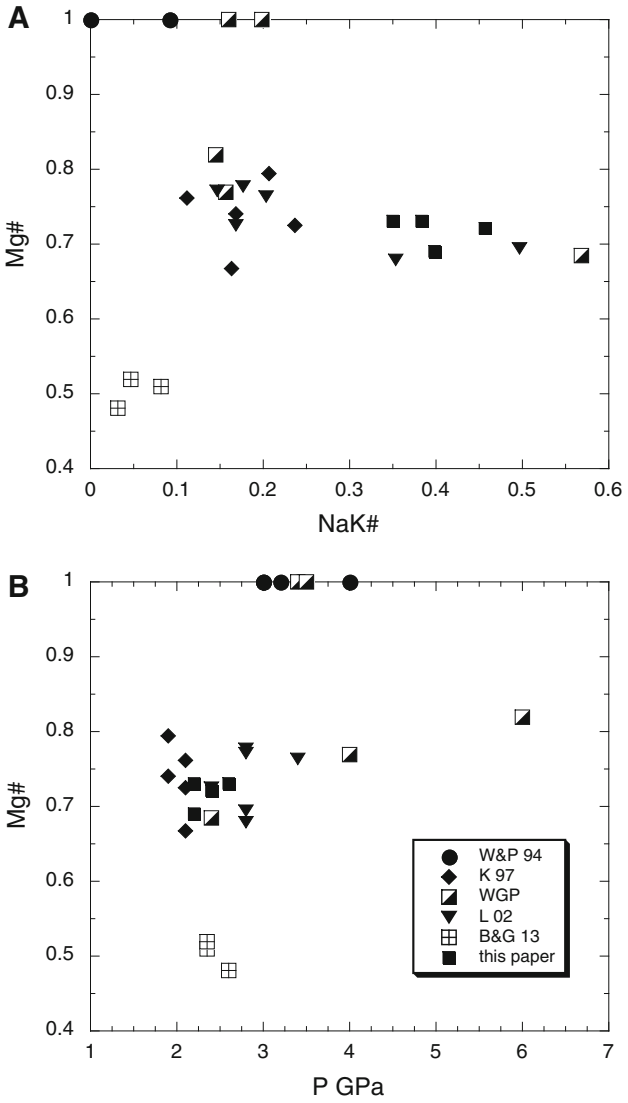

Fig. 6 Compositional characteristics of liquids in equilibrium with garnet lherzolite (oliv + opx + cpx + gar) phase assemblage. These data were used as inputs into the regressions for mineral components, temperature and pressure. **a** Mg# versus NaK#. **b** Pressure versus Mg#. The *symbols* refer to the studies of Walter and Presnall (1994) (W&P), Kinzler (1997), (K 97), Walter (1998) and Gudfinnsson and Presnall (1996), (WGP), Longhi (2002), (L 02), Barr and Grove (2013), (B&G 13) and this paper

data in our model were acquired. We do not have the means to resolve these differences.

Walter and Presnall (1994) and Gudfinnsson and Presnall (1996) report experiments from the mantle-analog CMAS ($CaO–MgO–Al_2O_3–SiO_2$) and CMASN (CMAS + Na_2O) systems, and all other studies used natural compositions. In Fig. 6a, the compositional variability spanned by these experimental liquids is illustrated using two key compositional variables, Mg# (molar Mg/[Mg + Fe^{2+}]) and NaK# (wt% [Na_2O + K_2O]/[Na_2O + K_2O + CaO]) that will be used in the following section to develop a model for predicting melt compositions in equilibrium with garnet lherzolite of variable composition. Also shown is the pressure range covered by the experimental data set (Fig 6b). Data coverage is concentrated on an Mg# range relevant for melting of depleted and metasomatized Earth mantle compositions, and the pressures extend from the spinel/garnet stability field boundary (1.9–2.2 GPa) to a maximum pressure of 6 GPa (Fig. 6b).

Mantle melting models for the natural plagioclase and spinel lherzolite have been developed by Kinzler and Grove (1992a, b), Kinzler (1997) and Till et al. (2012) by taking advantage of the constraint that four-phase CMAS peridotite-analog melting (forsterite + enstatite + diopside ± anorthite ± spinel ± pyrope) is a univariant equilibrium. Therefore, the composition and temperature of a

pure CMAS lherzolite melt is uniquely determined if pressure is specified. These three models chose to extend the constraints provided by this low-variance equilibrium to higher variance natural composition systems, taking advantage of the constraints provided by the Gibbs method. The number of compositional degrees of freedom in the natural lherzolite system is given by the Gibbs phase rule ($F = c + 2 - \Phi$), where F is the number of degrees of freedom, c is the number of components and Φ is the number of phases. In the lherzolite melting system $\Phi = 5$, giving the $F = 1$ (univariant) constraint for CMAS ($c = 4$). Walter and Presnall (1994) developed such a model for simplified plagioclase, spinel and garnet lherzolite in the CMASN system, where the melting becomes divariant ($F = 2$), requiring that a compositional variable be specified in order to predict melt composition. Following this approach, Till et al. (2012) extended the univariant constraint imposed by the CMAS system into the natural system.

In the garnet lherzolite model presented here, the number of components is 9 (CaO, MgO, FeO, Al_2O_3, SiO_2, Na_2O, K_2O, TiO_2 and P_2O_5) and there are 5 (or 6) phases involved (olivine, orthopyroxene, clinopyroxene, garnet, liquid and ±spinel); therefore, the thermodynamic variance of the system is 6 (or 5). Therefore, pressure and 5 (or 4) compositional variables need to be specified to predict the compositions of natural garnet lherzolite melts. Kinzler and Grove (1992a, b), Kinzler (1997) and Till et al. (2012) have identified Mg#, NaK#, K_2O and TiO_2 as components that systematically affect the compositions of lherzolite melts. After extensive testing of the effects of different compositional variables on garnet lherzolite melting, we found a set of 3 compositional parameters (1-Mg#, NaK# and P_2O_5) and pressure (P in kilobars) that reproduced most of the experimental diversity in melt compositions for our Gibbs phase rule inspired empirical model.

We chose to represent our experimental melt compositions with the oxygen-based mineral components Olivine (Oliv), Clinopyroxene (Cpx), Plagioclase (Plag) and Quartz (Qtz) following Kinzler and Grove (1992a). These components are the dependent variables in our model equations along with T (°C) and P (kbar) (Table 4). These components vary systematically from the CMAS univariant constraints and capture the important influence of Fe–Mg and Ca–Na–K exchange on the melting equilibrium. The input major element experimental data was recalculated using the Tormey et al. (1987) mineral component model. The experimental liquids, expressed in terms of the independent variables, P, 1-Mg#, NaK# and P_2O_5, were used to calculate the dependence of each mineral component on the independent variable using least-squares linear regression analysis. The model coefficients along with the errors on each dependent variable and the goodness of fit for each expression (r^2) are compiled in Table 4. Figure 7 shows

Table 4 Mineral component model equations for liquids saturated with an Olivine + Orthopyroxene + Clinopyroxene + Garnet lherzolite residue

	Intercept	(P − 1)	(1-Mg#)	NaK#	P_2O_5	r^2
T (°C)	1,313.67	8.423	−149.92	55.02	−59.69	0.90
	31	*0.85*	*46*	*68*	*26*	*24*
Oliv	0.1695	0.0053	0.2275	−0.1262	−0.0417	0.88
	0.02	*0.0005*	*0.03*	*0.04*	*0.02*	*0.01*
Plag	0.7439	−0.0095	−0.3878	0.5626	−0.12	0.93
	0.03	*0.0007*	*0.04*	*0.06*	*0.02*	*0.02*
Cpx	0.1268	0.00148	0.0874	−0.0525	−0.0376	0.53
	0.03	*0.0006*	*0.04*	*0.05*	*0.02*	*0.02*
Qtz	0.0024	0.00146	0.0146	−0.4425	0.0364	0.89
	0.02	*0.0006*	*0.03*	*0.05*	*0.02*	*0.02*

	Intercept	Oliv	(1-Mg#)	NaK#	P_2O_5	r^2
P (kbar)	−17.3	146.4	−38.4	19.6	4.81	0.84
	5.7	*15.9*	*5.1*	*7.9*	*3.2*	*2.3*

Numbers in italics are errors on coefficients. r^2 = correlation coefficient, and number below is average absolute error. *P* in kbar

the difference between the input variables (temperature, pressure and mineral components) and the values predicted by the model. A garnet lherzolite liquid barometer was also calculated using the Oliv mineral component as the independent variable following Till et al. (2012) who found that this mineral component reproduced the experimental pressures of the input data set with the smallest average error. The model coefficients for the barometer are compiled in Table 4.

Spinel: garnet phase boundary

The pioneering work of O'Hara et al. (1971) and MacGregor (1965) established the pressure–temperature conditions of the transition from spinel to garnet lherzolite facies at subsolidus conditions, and many subsequent papers have explored the pressure dependence of the transition and the influence of variable Fe/Mg and Cr_2O_3 (see O'Neill 1981 for a review of early work). At temperatures well below the anhydrous solidus (~1,000 °C), the spinel/garnet boundary occurs at nearly constant pressure, but near the solidus, the boundary changes slope dramatically (Klemme and O'Neill 2000; Walter and Presnall 1994; Walter 1998). Our data set on garnet lherzolite-saturated melts allows a characterization of the pressure–temperature—compositional dependence of this phase transition above the solidus region. The effect of variable Na_2O on the spinel/garnet boundary is well characterized in the CMASN system, where the melting reaction is univariant (Walter and Presnall 1994). Our new experimental data, that of Barr and Grove (2013) and Walter and Presnall (1994), expands

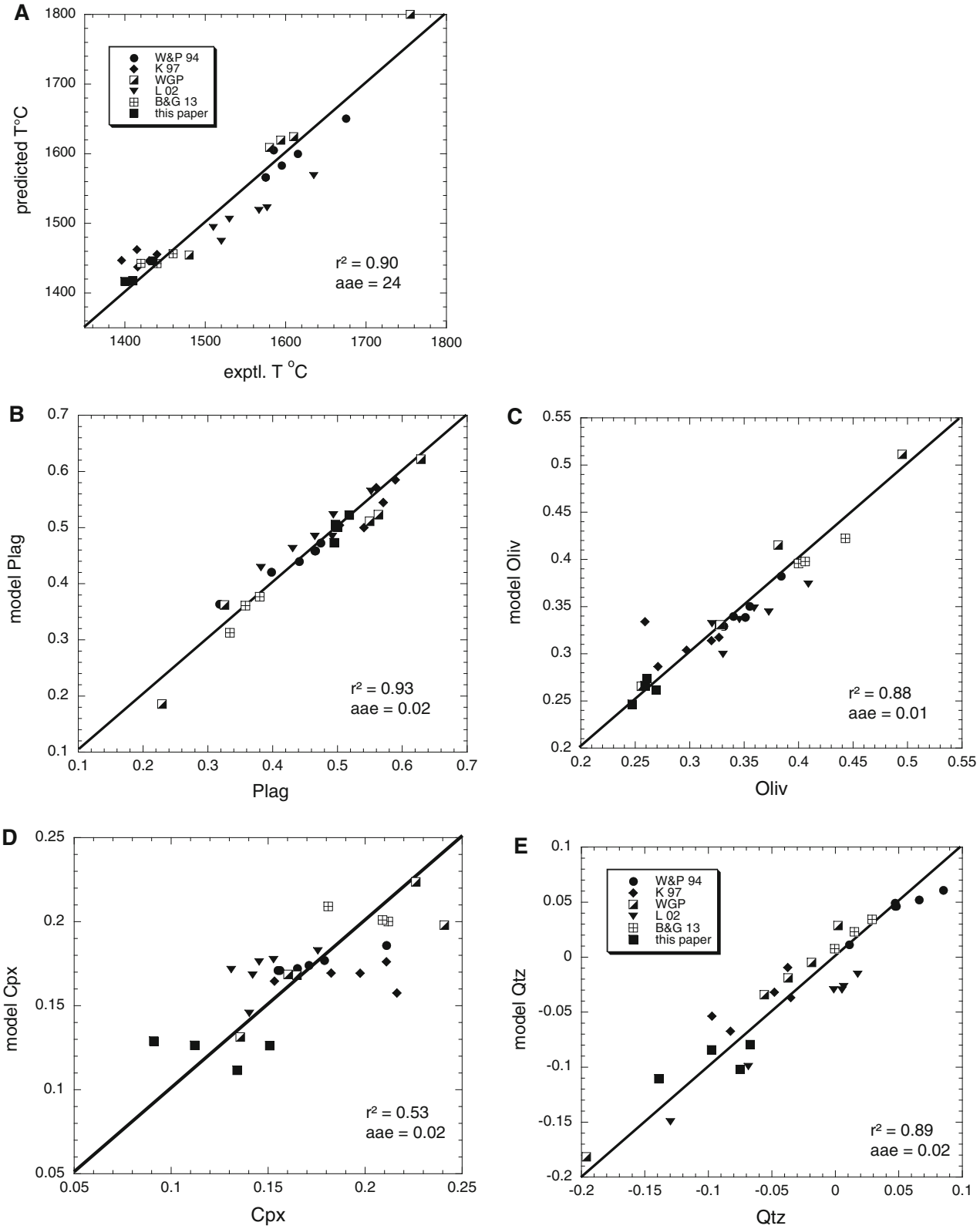

Fig. 7 Experimental versus predicted values of temperature and mineral component values for the garnet lherzolite-saturated liquids used in the temperature and mineral component models for the variation in composition of the garnet lherzolite MSP. Black line indicates 1:1 correspondence of experimental and calculated values. *Symbols* are the same as in Fig. 6. Values in the lower right show the square of the correlation coefficient (r^2) and one sigma average absolute error of the fitted values (aae)

the compositional range to both high iron and higher $Na_2O + K_2O$ compositions. The compilation of relevant experimental data includes ten experiments that contain both spinel and garnet (Table 3). We have used these to generate a model of the pressure and temperature dependence of the phase transition. We calculated the pressure and temperature dependence of the boundary for two variables (Mg# and NaK#) that previous workers have shown to exercise important controls on temperature and pressure. The expressions are:

$$P\,(\text{in GPa}) = 1.2 - 0.52\,(\text{NaK\#}) + 2.11\,(\text{Mg\#})$$
$$r^2 = 0.81$$

$$T\,(\text{in }^\circ\text{C}) = 1,250 - 227\,(\text{NaK\#}) + 353\,(\text{Mg\#})$$
$$r^2 = 0.90$$

The fit and the experimental data are shown in Fig. 8 along with the pressure temperature dependence of the spinel–garnet phase boundary for constant NaK# (0.2) and variable Mg# (from 0.5 to 1.0). The input data fall close to the plane calculated for the phase boundary (±0.1 GPa brackets on the fit are also plotted), and the width of the phase transition in this high-variance natural system is ~0.2 GPa. The experiment that plots well away from the predicted line (by 0.3 GPa) is the CMAS spinel/garnet invariant point from Walter and Presnall (1994). We have no explanation for this discrepancy, because the high-pressure–temperature–Mg# end of the line is defined by the Walter and Presnall (1994) experiments in CMAS + Na_2O.

A variable that cannot be explored with our garnet lherzolite liquid data is the influence of Cr_2O_3 on the width of the transition. O'Neill (1981) showed that the addition of Cr_2O_3 created a fairly broad pressure interval over which spinel and garnet could coexist, and this is likely to be the situation when Cr-rich spinel is present in the lherzolite. Because of its refractory nature, it is likely that a Cr-rich spinel would not participate in the silicate melting reaction. At this time, there is not sufficient data above the solidus to explore this possibility, and further experimental study would be necessary in order to evaluate the effects of variable Cr_2O_3.

Conditions and compositional characteristics of peridotite melts in the garnet, spinel and plagioclase facies

The garnet lherzolite melting model can be combined with melting models in the spinel and plagioclase lherzolite facies to predict the temperature and pressure of a melt of a given composition in the stability field of each lherzolite facies. These models also predict melt composition for peridotites of variable composition if pressure and compositional characteristics of the lherzolite source are specified.

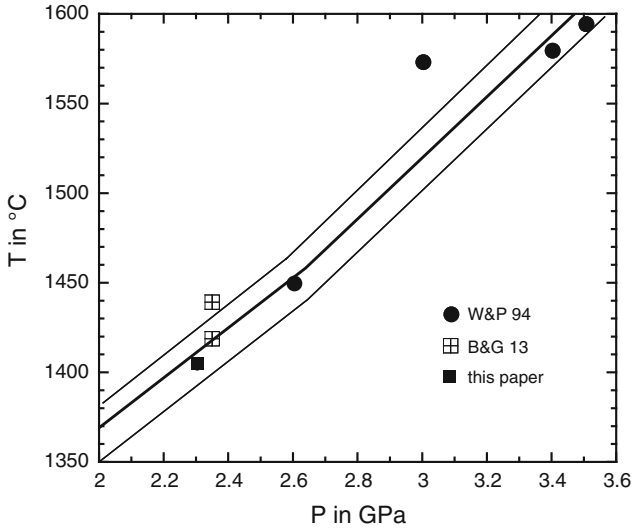

Fig. 8 Pressure versus temperature plot of spinel + garnet-saturated lherzolite melts. Data are from this study, Barr and Grove (2013), Walter and Presnall (1994) (abbreviated W&P 94) and Kinzler (1997). Also shown is the fit to the supersolidus spinel to garnet lherzolite phase transition discussed in the text. The *line* was calculated by holding NaK# constant at 0.2 and varying the Mg# from 1.0 to 0.5. The single point that plots away from the calculated boundary is a CMAS experiment with NaK# = 0.0, Mg# = 1.0 from Walter and Presnall (1994). The remaining experimental liquids have NaK# that varies from 0.10 to 0.30. Mg# is the primary source of pressure–temperature variations in this input data set, varying from 0.5 to 1.0. The 3 data used in the fit from Kinzler (1997) at 1.9 GPa are not shown on the plot

Till et al. (2012) present an updated model for melting of compositionally variable plagioclase and spinel lherzolite along with a prediction of the spinel/plagioclase phase transition. In the following discussion, we will use their models along with the garnet lherzolite model presented here to explore the compositional characteristics of melts from metasomatized peridotite compositions.

Correcting for fractional crystallization: an essential first step

An essential first step in estimating the conditions of melting for suspected mantle derived magma is to correct for the effects of fractional crystallization that operate to evolve the magma away from its original composition. This issue has been discussed in previous papers (Kinzler and Grove 1992a, b; Kinzler 1997; Till et al. 2012) and that discussion will not be repeated here, except to emphasize that the assumptions made in correcting evolved basaltic melts for the effects of fractional crystallization can have significant effects on the temperature, pressure and composition inferred for the predicted primary melt composition. In particular, the assumption that an evolved liquid has been modified by olivine-only fractional crystallization

when it actually experienced a multiphase fractional crystallization process (see Till et al. 2012, their Fig. 6) can lead to large errors in predicting the temperature, pressure and composition of a primary melt. Worked examples in the following section will discuss the reasoning that has been applied to two natural examples.

Application to tertiary magmatism in the Tibetan plateau

High potassium basaltic lavas have been erupted on the Tibetan Plateau during its entire history of uplift that extends through the Tertiary (63–3 million years before present, Ding et al. 2003; Guo et al. 2006; Nomade et al. 2004; Williams et al. 2004). Holbig and Grove (2008) carried out experiments on one of these lavas (Bb-107, Williams et al. 2004) and placed constraints on the possible fractional crystallization processes that these magmas could have experienced as they passed through the thick crust beneath the Plateau on their way to the surface. Holbig and Grove (2008) found evidence for high-pressure fractional crystallization in Bb-107 involving olivine + clinopyroxene. The experiments reported here on the BbGtOpx were initiated so that a quantitative model for peridotite melting could be developed in order to understand the temperature, pressure and melting history of these lavas. The major trace element and isotopic compositions of the high-K Tibetan lavas have been reported (Ding et al. 2003; Guo et al. 2006; Nomade et al. 2004; Williams et al. 2004). Their mantle sources have been proposed to be phlogopite-bearing metasomatized lherzolites, and trace element models conclude that the sources of these lavas are at depths near the spinel to garnet facies transition. Therefore, the Tibetan lavas provide an excellent test of the garnet lherzolite melting model.

The basaltic lavas analyzed by Ding et al. (2003), Guo et al. (2006), Nomade et al. (2004) and Williams et al. (2004) were corrected by reverse fractional crystallization (33 compositions in total, see electronic supplementary material, ESM Table 1). Several lavas are very close to being primary magmas in equilibrium with a lherzolite source and required only small amounts of olivine addition to bring them into equilibrium with a mantle source (assumed to contain olivine with a composition of $Fo_{90.5}$). Other lavas are more evolved and plot at silica-undersaturated compositions along a trend that implies olivine + clinopyroxene and/or olivine + clinopyroxene + plagioclase fractional crystallization. Reverse fractional crystallization models using these phases were also applied to some of the compositions (ESM Table 1). We used the techniques of Yang et al. (1996) to perform the reverse fractionation and assumed pressures in the range inferred by Holbig and Grove (2008) for Bb-107 (1.4–2.2 GPa).

The compositional characteristics of the Tibetan near-primary liquids show a range of alkali contents that result in a range of NaK# values from 0.226 to 0.290, P_2O_5 values ranging from 0.13 to 1.32 wt% and an Mg# value of 0.732. Primary melts of mantle lherzolite with these characteristics were predicted using the plagioclase and spinel models (Till et al. 2012) and the garnet lherzolite model (Table 4) and they are plotted in Fig. 9. The three segments of each trend show the change in composition of MSPs for the plagioclase, spinel and garnet lherzolite facies with increasing pressure. The plagioclase lherzolite MSPs are calculated over the pressure range of 0.001–12 kilobars, spinel lherzolite MSPs are calculated from 12 to 24 kilobars and garnet lherzolite MSPs are calculated from 24 to 40 kilobars. Discrete MSP values are indicated by their pressure at 4 kilobar intervals in Fig. 9. The fractionation-corrected Tibetan lavas are plotted in Fig. 9 using two symbols; circles and squares. Of the 33 corrected high-K basaltic lavas in the data set, 15 plot in the vicinity of the spinel and garnet lherzolite MSPs (black circles). These 15 lavas fall on or near the same MSP pressure on all 3 subprojections. The remaining lavas (gray squares) plot at compositions that are more SiO_2-undersaturated (negative Qtz values on the Oliv − Plag − Qtz and Oliv − Cpx − Qtz subprojections) than the spinel and garnet MSPs on the Oliv − Plag − Cpx subprojection. These remaining 18 compositions lie along Oliv + Cpx + Gar/Spinel saturation boundaries that extend down temperature from the MSPs and thus they represent liquid compositions that are not saturated with spinel or garnet lherzolite. These lavas may represent primary magmas that originally were saturated with garnet lherzolite but upon separation from the source region, ascended into cooler overlying mantle and experienced fractional crystallization along the Oliv + Cpx + Gar/Spinel boundary relevant for their depth of crystallization. However, since these melts have already been corrected for fractional crystallization to Fo_{90}, it is more likely they represent melts of a non-lherzolitic mantle lithology such as Oliv − Cpx − Gar/Spinel veins in heterogeneous peridotite. Melting of this veined source could simultaneously produce melts of these varying compositions during the same melting process that gave rise to the lherzolite-saturated near-primary melts. Alternatively, these liquids could be melts segregated from mantle veins that were produced by down-temperature fractional crystallization of liquids separated from a mantle source. These liquids were delivered to shallower, cooler depths in the mantle where they crystallized and left Oliv − Cpx − Gar/Spinel residues.

There are no obvious geographical or temporal signals in the distribution of the primary magmas to suggest the scale of the mantle heterogeneity. The lavas come from the N. Qiantang and Songpan-Ganzi terrains and range in age

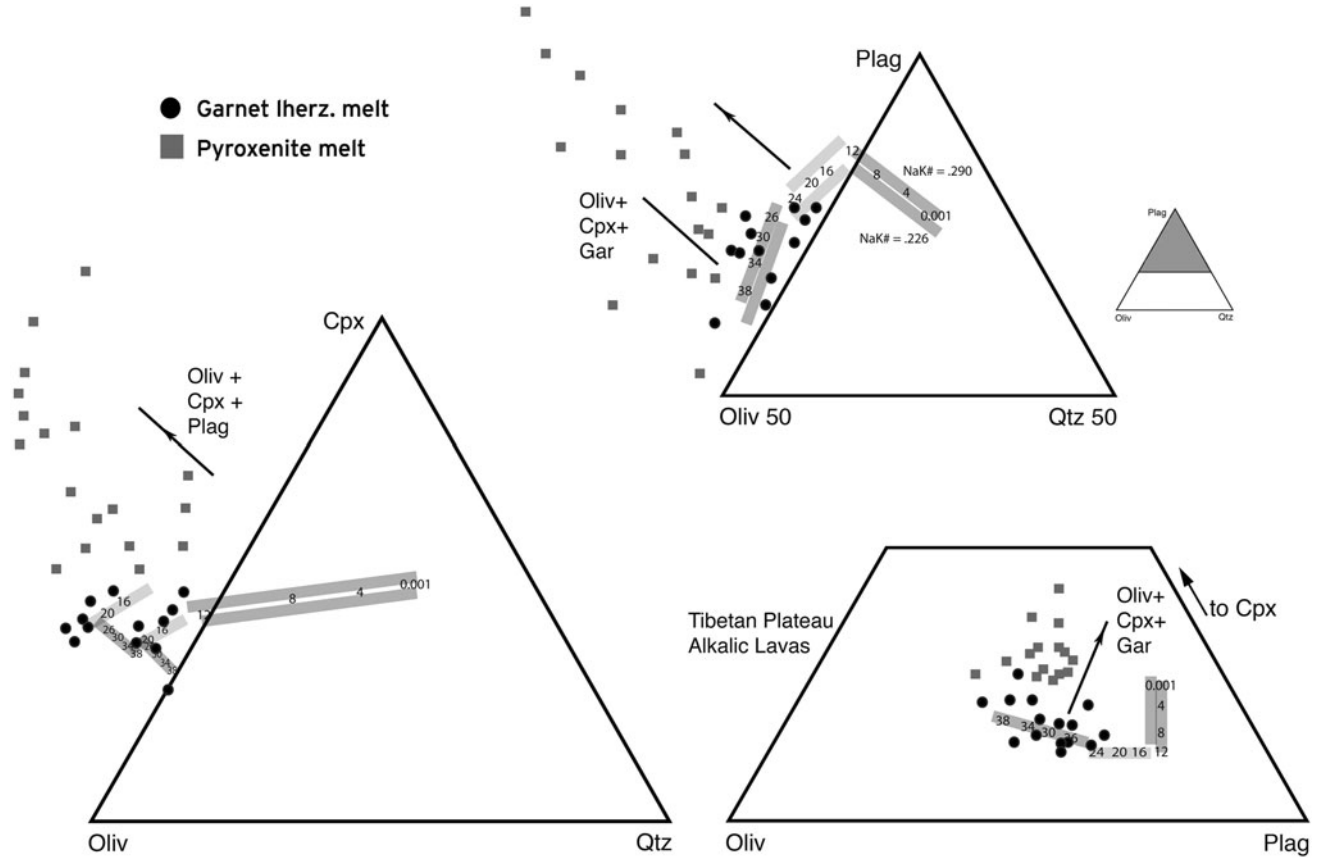

Fig. 9 Pseudoternary subprojections (Tormey et al. 1987, oxygen units) showing compositions of fractionation-corrected lavas from the Tibetan Plateau. Also shown are the predicted plagioclase, spinel and garnet lherzolite MSPs as a function of increasing pressure for 1 atmosphere (0.001 kbar) to 40 kbar. Predictions are shown for Mg# = 0.73 NaK#s of 0.226 and 0.290, the range of alkali contents spanned by the corrected data set. The plagioclase and spinel lherzolite MSPs are calculated using Till et al. (2012), and garnet lherzolite liquids are calculated using the model in Table 4. Also shown schematically is the trend followed during oliv + cpx + gar/spinel down-temperature crystallization when liquids leave the spinel or garnet MSPs. Also shown are fractionation-corrected compositions of Tibetan lavas using black circles and gray squares. Corrected compositions are found in electronic supplementary material. Lavas indicated with *black circles plot* near spinel and garnet lherzolite MSPs. Lavas indicated by *squares* lie on Oliv + Cpx + Gar/Spinel saturation boundaries are pyroxenitic

from 63 to 6.4 million years. Also, there are no systematics in the incompatible trace element, rare earth element and isotopic compositions of the spinel- and garnet lherzolite-saturated magmas (circles in Fig. 9) that distinguish them from the high-pressure Oliv − Cpx − Gar/Spinel- evolved melts/fractionates (squares in Fig. 9). All authors who have studied these Tibetan lavas conclude that there was significant heterogeneity in their mantle source regions for the incompatible trace and rare earth elements. There are systematic differences in the compatible elements. Both Ni and Cr concentrations are significantly higher in the garnet and spinel lherzolite-saturated primary magmas and lower in the Oliv − Cpx − Gar/Spinel-evolved melts/fractionates. The low Ni in the Oliv − Cpx − Gar/Spinel melts could result from reaction between melts of pyroxenite veins with overlying peridotite mantle with Ni preferentially remaining in the mantle residue (Sobolev et al. 2005). The evidence from major element MSP analysis confirms the conclusions of trace element modeling that place the depth of origin near the garnet–spinel facies boundary (Fig. 9) and furthermore suggests the presence of both lherzolitic and garnet pyroxenitic source regions for the Tibetan lavas.

Distinguishing lherzolite melts from pyroxenite melts

The question of whether the source region for a basaltic melt is lherzolite or pyroxenite remains a topic of active discussion and debate. Because lherzolite is the dominant rock type in the mantle, partial melting of this rock type has been assumed to be the origin for most basaltic melts. However, other source materials are present in the mantle, and these could also melt to produce basalts. Pyroxenite is a minor but omnipresent component among mantle samples, and it is possible that melting sometimes involves this component of the mantle [see Pertermann et al. (2004) for a

review]. Phase equilibrium studies have been performed on a variety of pyroxenitic mafic compositions at high pressures to determine the compositional characteristics of the melts of pyroxene-bearing lithologies (Takahahshi et al. 1998; Kogiso et al. 1998, 2003, 2004; Hirschmann et al. 2003). The results of these studies can be compared with the predicted melt compositions of lherzolite sources to see whether major element characteristics discriminate pyroxenite melting from lherzolite melting.

The compositions of pyroxenitic melts from the experimental studies of Takahahshi et al. (1998), Kogiso et al. (1998, 2004), Hirschmann et al. (2003) and Pertermann et al. (2004) are plotted in pseudoternary composition space in Fig. 10. The MSPs for high Mg# melt compositions (Mg# = 0.69, NaK# = 0.37) from Kogiso et al. (2003) were predicted using the plagioclase and spinel lherzolite models (Till et al. 2012) and the garnet lherzolite model, and they are also plotted in Fig. 10. These predicted MSP liquids used the high Mg# end of melt compositions that are present in the input data set, but the alkali contents and Mg# variation of the data set do not vary significantly, and the changes in the position of the MSP over this range of composition will be small. Kogiso et al. (2004) discuss the existence of a thermal divide in their compositional analysis of garnet pyroxenite melting that separates SiO_2-undersaturated pyroxenite melts that are olivine-normative from SiO_2-enriched melts that are sometimes quartz-normative. It is also true that there is much more than just a thermal divide within the region that lies between the SiO_2-poor and SiO_2-rich melts. The region that separates these compositions contains the part of composition space where melts of plagioclase, spinel and garnet lherzolite melts occur.

In the three subprojections of Fig. 10, the SiO_2-undersaturated olivine-normative pyroxenite melts are indistinguishable from the Oliv − Cpx − Gar/Spinel-evolved melts/fractionates like those from the Tibetan plateau. These melts/fractionates lie on Oliv + Cpx + Garnet/Spinel + liquid boundaries that extend down temperature from the spinel and garnet MSPs, and the boundaries lie on the SiO_2-undersaturated side of the thermal divide. The experimental liquids that plot on the other side of Kogiso et al. (2004) thermal divide plot at high values of Qtz and

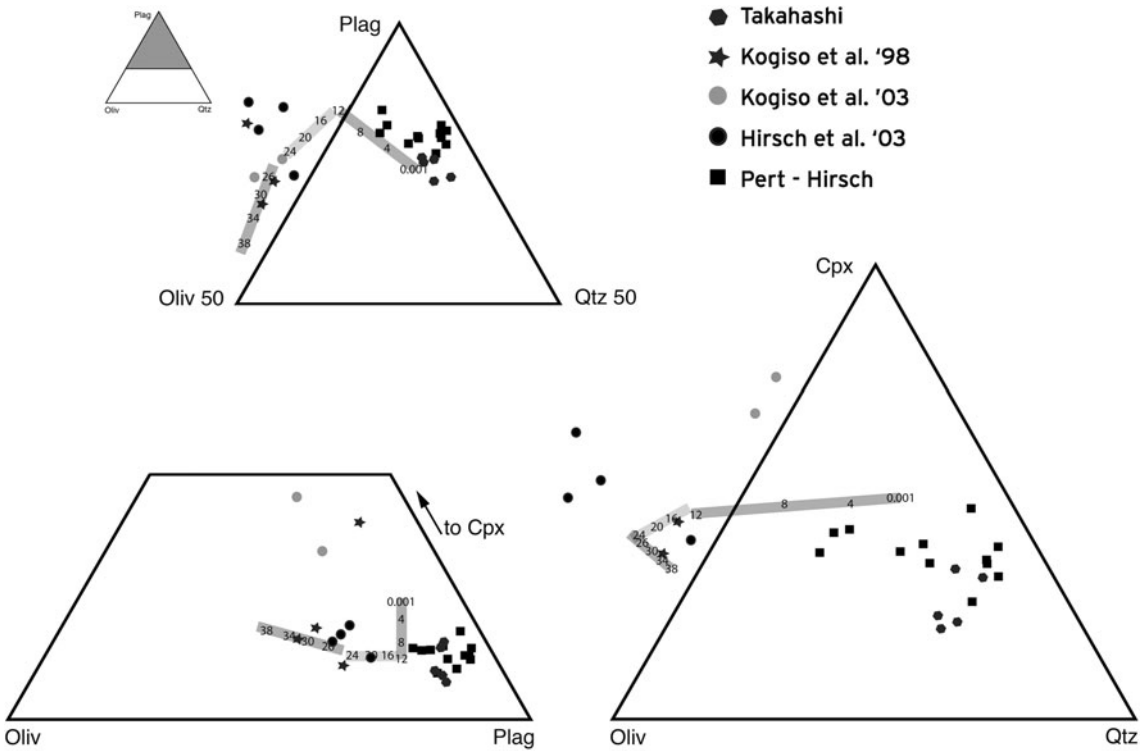

Fig. 10 Pseudoternary subprojections showing compositions of experimentally produced pyroxenite-saturated melts from the literature. Projection schemes are the same as that used in Fig. 9. The pyroxenite *liquids plotted* here vary widely in compositional characteristics, but separate into two groups: quartz-normative and nepheline-normative (SiO_2) undersaturated. The silica-undersaturated liquids lie on oliv + cpx + garnet saturation boundaries. Also shown are the predicted plagioclase, spinel and garnet lherzolite MSPs as a function of increasing pressure for 1 atmosphere (0.001 kbar) to 40 kbar. Plagioclase lherzolite MSPs are calculated over the pressure range of 0.001–12 kilobars, spinel lherzolite MSPs are calculated from 12 to 24 kilobars and garnet lherzolite MSPs are calculated from 24 to 40 kilobars. These MSPs were calculated for a liquid with compositional characteristics similar to the Kogiso et al. (2003) liquids using Till et al. (2012) and the model in Table 4. Note, several of the points of Kogiso et al. (1998) are very SiO_2-undersaturated and plot at negative quartz values that are outside of the range of composition space shown

Plag in all three subprojections. These SiO_2-enriched liquids lie closest to the region of composition space where basaltic melts that have experienced low-pressure fractional crystallization would plot. This is to be expected since many of these compositions were produced from melting-evolved basaltic compositions (e.g., a MORB protolith). Neither the SiO_2-enriched or SiO_2-undersaturated pyroxenite melts plot near the MSPs for the spinel or garnet facies in any of the subprojections. The predicted compositions of the spinel and/or garnet MSPs may provide a useful means for distinguishing between melts of lherzolite versus pyroxenite source regions. In Fig. 10, two data points from Kogiso et al. (1998) partly coincide with the MSP trend. Those two liquids from Kogiso et al. (1998) are melts of peridotite + basalt mixtures that are probably not far-removed from the composition of a multiply saturated melt. All other compositions plot well away from the MSPs: a distinguishing characteristic of pyroxenite melts. The predicted compositions of the spinel and/or garnet MSPs thus are a potential means for distinguishing between melts of lherzolite versus pyroxenite source regions.

Effects of CO_2 on garnet lherzolite melts: an example from early Kilauea

Another process to consider in the origin of garnet lherzolite melts is the effect of CO_2 on the melt composition. It has been well established that the presence of CO_2 lowers the SiO_2 content of peridotite melts (Kushiro 1975; Brey and Green 1975; Wyllie and Huang 1976; Eggler 1978). These early studies established the broad compositional changes caused by the presence of CO_2 and showed that melts of carbonated source regions have compositional characteristics similar to nephelinites, basanites and melilitites. Recent experimental studies have focused on the highly alkalic and CO_2-rich partial melts (Thibault et al. 1992; Hirose 1997; Dasgupta and Hirschmann 2006, 2007; Dasgupta et al. 2007). The melt compositions produced in the experiments on carbonated lherzolite at pressures within the garnet stability field show a continuous variation from nearly SiO_2- and Al_2O_3-free carbonatite to SiO_2-undersaturated nephelinites. Compositions of these CO_2-bearing nephelinitic melts that are in equilibrium with a garnet lherzolite assemblage (Thibault et al. 1992; Dasgupta et al. 2007) are plotted in Fig. 11 along with the composition of garnet and spinel lherzolite MSPs with similar melt characteristics (NaK#, Mg#). The Oliv − Cpx − Qtz and Oliv − Plag − Qtz subprojections are not shown for these carbonated lherzolite melts because they are strongly silica undersaturated and plot at negative Qtz values of −0.5 and greater.

Nephelinitic lavas often have high concentrations of phenocrystic olivine making it difficult to know whether the bulk rock composition is that of a melt or melt + accumulated olivine. Sisson et al. (2009) characterizes nephelinite and basanite glass grains preserved in sandstone blocks from early Kilauea that are unquestionably quenched liquid compositions. These highly silica-undersaturated nephelinites and basanites contain SiO_2 contents as low as 38 wt% and total alkali ($Na_2O + K_2O$) contents of 10.5 wt%. Sisson et al. (2009) apply a reverse-fractionation correction by adding olivine back into the glass composition until the liquid is in equilibrium with $Fo_{91.5}$ olivine. They summarize evidence for the involvement of CO_2 in melt generation processes at Hawaii and propose that these melts are produced at or near the base of the lithosphere beneath Hawaii (~3 GPa) as near solidus melts of carbonated phlogopite-bearing garnet lherzolite. The compositions of these fractionation-corrected glasses are also plotted in Fig. 11. Melts of carbonated garnet lherzolite can be readily distinguished from CO_2-free garnet lherzolite and Oliv − Cpx − Gar/Spinel-evolved melts/fractionates by their enrichment in Cpx component and their extreme silica undersaturation. More experimental data would be necessary at variable CO_2 melt concentrations in order to quantify the influence of varying CO_2 on the garnet lherzolite MSPs.

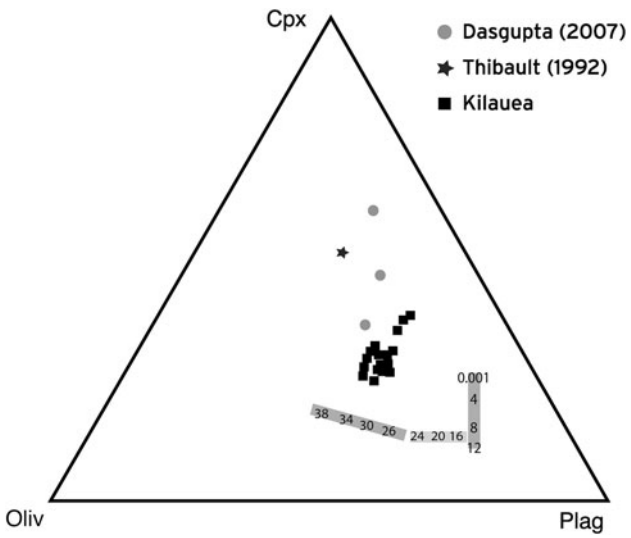

Fig. 11 Oliv − Plag − Cpx pseudoternary subprojection showing compositions of experimentally produced liquids saturated with carbonated, K-rich garnet lherzolite melts from Thibault et al. (1992) and Dasgupta et al. (2007). Also shown are the fractionation-corrected nephelinite–basanite liquids from submarine eruptions on Kilauea's south flank (Sisson et al. 2009). Sisson et al. (2009) propose that these liquids were derived from a carbonated phlogopite-bearing garnet peridotite. These CO_2-rich garnet lherzolite melts are compositionally distinct from CO_2-free, anhydrous melts of high-K garnet lherzolite. MSP for CO_2-free melts saturated with plagioclase, spinel and garnet lherzolite are shown for liquids with the compositional characteristics of the Sisson et al. (2009) glasses calculated over the pressure range of 0.001–40 kilobars (see Fig. 10 caption). Projections involving the Quartz component are not shown, because the carbonated garnet peridotite melts are extremely silica undersaturated and plot far away from the CO_2-free garnet lherzolite MSPs

Alkali basalts and tholeiites from Hawaiian volcanoes: peridotite versus pyroxenite sources

The nephelinites and basanites associated with the early stages of Hawaiian volcanism are rare and unusual magmas. More abundant are ordinary alkali and transitional basalts that precede and postdate shield growth (Moore et al. 1982; Clague 1987; Sisson et al. 2002), and shield-stage tholeiites that constitute most of the volume of Hawaiian volcanoes. A long-standing issue in Hawaiian magmatism has been the origin of the voluminous shield-stage tholeiites. That they fractionate from picritic parents was resolved by the discovery of picritic tholeiite glass grains near Kilauea's submarine Puna Ridge (Clague et al. 1995). Trace element systematics point to residual garnet at some stage in their generation (Hofmann et al. 1984), as would be expected for the ~80 km thickness of ~90 Ma Pacific Plate lithosphere in the Hawaii region, but even their inferred picritic parents are higher in SiO_2 than would be expected for melts of garnet lherzolite sources. To account for their high SiO_2, as wells as high Ni concentrations in Hawaiian olivine phenocrysts, Sobolev et al. (2005) propose that more than half of Hawaiian magmas came from an olivine-free pyroxenitic sources.

To assess whether major element evidence supports this hypothesis, we have accumulated 1,675 submarine glass analyses from the literature for Kilauea (Coombs et al. 2004; Clague et al. 1995; Naka et al. 2002), Mauna Loa (Garcia et al. 1989, 1995; Moore et al. 1985; Moore and Clague 1987) and Loihi (Clague et al. 2000; Garcia et al. 1995; Moore et al. 1982). We filtered these glasses first to include only those with MgO >6.5 wt%, retaining 780 analyses, and then, further screened these to exclude liquids that experienced multiphase fractional crystallization by retaining only analyses with Mg# >55. For the remaining 143 glass compositions, a reverse-fractionation correction was applied by adding olivine back into the glass composition until the liquid is in equilibrium with Fo_{90} olivine (ESM Table 2). These near-primary melts have an Mg# value of 0.728 and NaK# near 0.18. Primary melts of mantle peridotite were predicted for these compositional parameters using the plagioclase, spinel and garnet lherzolite models and are plotted in Fig. 12 with MSP pressure noted. The fractionation-corrected glasses plot as two densely clustered arrays. The more populous of the two clusters (124 compositions) plots at normative Plag and Cpx values that are lower than the MSP arrays in the Oliv − Cpx − Qtz and Oliv − Plag − Qtz subprojections. These primary magma compositions plot coincident with olivine + orthopyroxene saturation boundaries in the pressure range of 1.4–1.0 GPa (Wagner and Grove 1998; Eggins 1992). The second cluster of 16 primary compositions plots at SiO_2-undersaturation and coincides with garnet lherzolite MSPs at ~3.2–3.6 GPa. Only three points plot in the portion of composition space occupied by olivine pyroxenite melts (one plots at very highly negative Qtz values and is not visible on the subprojections containing Qtz).

The predominate clustering of primary magmas on the oliv + opx boundary consists wholly of tholeiites. Their natural and fractionation-corrected compositions plot well below the SiO_2-total alkalis discrimination line of Macdonald and Katsura (1964) (not illustrated). Our proposed origin for these is that they were initially garnet-saturated melts from upwelling asthenosphere (depths of 80–90 km) that have ascended into mantle lithosphere beneath Hawaii and reacted with it by assimilating pyroxene and crystallizing olivine, resulting in melts in equilibrium with harzburgite residues at relatively shallow depths (Eggins 1992; Wagner and Grove 1998; Stolper et al. 2004). The subordinate group of fractionation-corrected basalts that cluster along the 3.2–3.6 GPa garnet lherzolite MSPs represent decompression melts of the asthenosphere generated in the plume that segregated near the base of the lithosphere (80–90 km depth) and ascended without appreciable subsequent wallrock reaction. These glasses are wholly from early Kilauea and Loihi, and their natural glass compositions plot (not illustrated) along the Macdonald and Katsura (1964) tholeiitic-alkalic discrimination line or short distances into the alkali basalt field. Thus, these magmas would be classified as transitional and weakly alkalic basalts. Common but more strongly alkaline Hawaiian basaltic glasses, including hawaiites, failed to pass the MgO and Mg# screens, consistent with their deriving mainly from multiphase fractionation at mantle lithosphere depths (Frey et al. 1990).

The primary transitional and weakly alkaline melts can be interpreted as the parents of the more abundant tholeiites that have escaped melt-wallrock reaction with shallower Hawaiian lithosphere. The overall scenario appears to be that at early growth stages of Hawaiian volcanoes, melts of garnet lherzolite and of carbonated garnet lherzolite arrive at the surface having undergone fractionation of olivine (shallow) or of olivine and pyroxene (deep), but with little melt-wallrock reaction. As magmatic flux increases and conduits warm, melt-wallrock reaction becomes common and deep fractionation of pyroxene-rich assemblages diminishes. Magmas with major element compositional characteristics of pyroxenite melts are truly the rare exception in Hawaii, and only 3 emerge from this analysis of major element characteristics. From this major element evidence, it appears that we must identify processes that can reconcile both the major and trace element signatures of Hawaiian lavas.

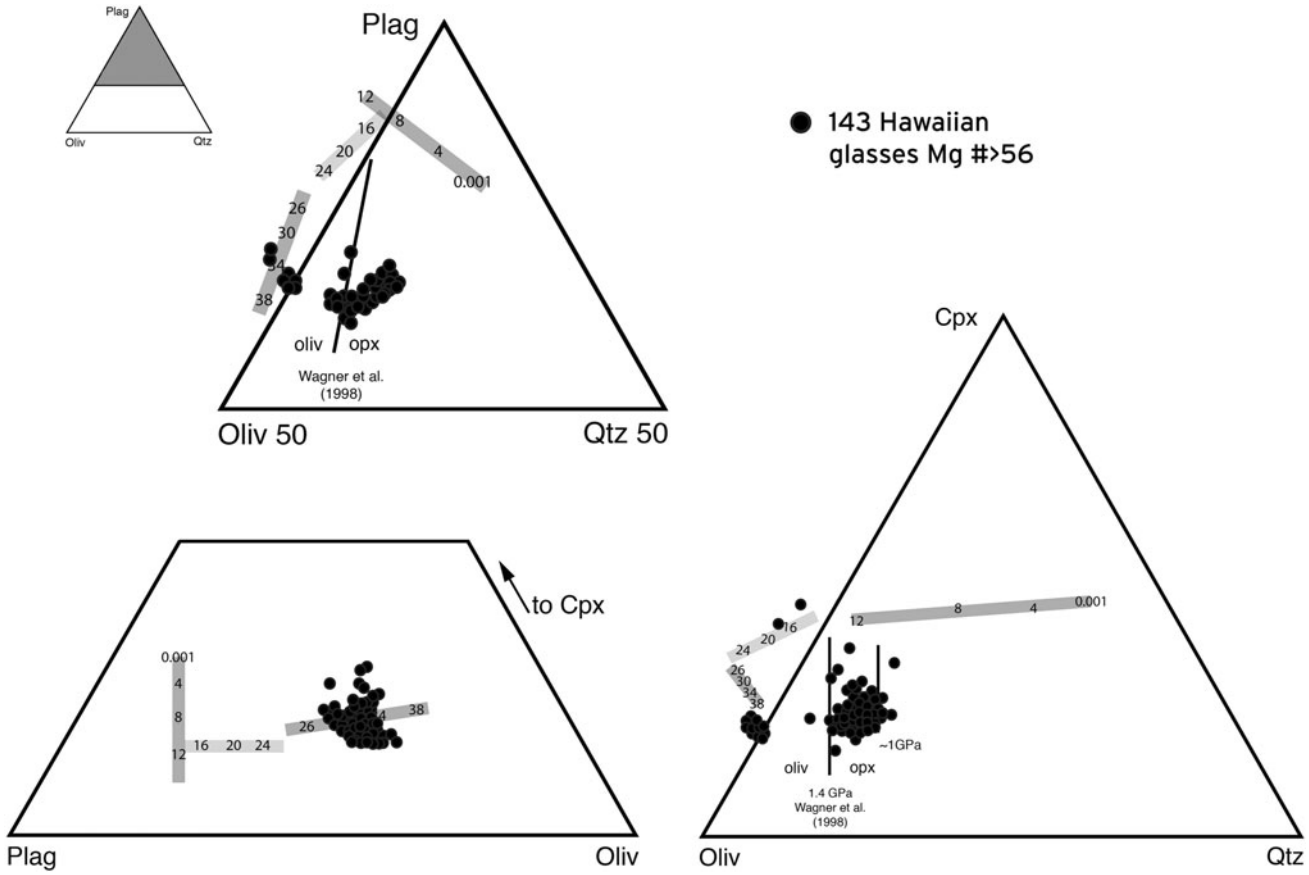

Fig. 12 Pseudoternary subprojections showing compositions of 143 glasses with Mg# between 0.56 and 0.70 from Kilauea, Mauna Loa and Loihi. These glasses were chosen from a larger data set (see text for data sources). Projection schemes are the same as Fig. 9. These glasses were all reverse fractionation–corrected by adding equilibrium olivine until the liquid was in equilibrium with Fo_{90} (data in ESM Table 2). Also shown are the predicted plagioclase, spinel and garnet lherzolite MSPs as a function of increasing pressure for 1 atmosphere (0.001 kbar) to 40 kbar. Plagioclase lherzolite MSPs are calculated over the pressure range of 0.001–12 kilobars, spinel lherzolite MSPs are calculated from 12 to 24 kilobars and garnet lherzolite MSPs are calculated from 24 to 40 kilobars. Calculation assumed an Mg# = 0.728 and NaK# = 0.18 (range of NaK# in data spans 0.16–0.2). Also shown in the Qtz-bearing projections is the oliv + opx saturation boundary experimentally determined at 1.4 GPa by Wagner and Grove (1998) for a primary Hawaiian tholeiite composition (Clague et al. 1995). In the Oliv-Cpx-Qtz subprojection, the position of the 1 GPa oliv + opx boundary is inferred from the predicted MSP data. The majority of the Hawaiian shield lavas (124 points) were derived from a harzburgite residue at 1.4–1 GPa. A smaller proportion of the magmas plotted originate just below the base of the Hawaiian lithosphere at 3.2–3.6 GPa as melts of garnet lherzolite. Only three lavas plot at higher negative values of Qtz (one is at very high negative Qtz values) in the region of composition space consistent with melting of an olivine pyroxenite source

Predicting melts of compositionally diverse mantle sources

Using a similar approach to Kinzler and Grove (1992a, b, 1993) and Till et al. (2012), we can model melting processes of compositionally diverse mantle sources by either batch or fractional melting. To model garnet lherzolite melting, we use the mineral component expressions for garnet facies melting (Table 4) and assume the garnet melting reaction derived by Kinzler and Grove (1999) (see Eq. 1 in their paper). To implement the model, the Mg# and composition of minor elements (Na_2O, K_2O, TiO_2 and P_2O_5) in each melt increment must be estimated. The non-modal batch melting equation, given below, is used to estimate these concentrations. Each source composition and an initial solidus mineral mode are input, and the compositions of opx and cpx from the model experimental data are used to recalculate this mode to the pressure and temperature conditions of melting.

$$C_i = C_0/(D_B + F(1 - P_B))$$

where C_i is the minor component abundance, C_0 is the abundance of the component in the bulk solid, D_B is the solid/melt partition coefficient for each phase multiplied by its weight fraction in the bulk solid, F is the melt fraction and P_B is the bulk solid/melt partition coefficient for the component weighted by the stoichiometric coefficients of the melting reaction. The calculations use weight units.

Partition coefficients have been calculated from the mineral and melt compositions that are incorporated in the major element melting model; pressure-dependent partition coefficients are modeled for Na_2O and TiO_2 in orthopyroxene and clinopyroxene and following Kinzler (1997) (Table 4). Other partition coefficients are constant and are from Kinzler (1997).

Following the method of Kinzler and Grove (1993), the Mg# of a melt coexisting with a lherzolite composition is determined by solving equations for the conservation of mass for FeO and MgO between the minerals in the lherzolite and a given fraction of melt. The method requires knowledge of the partitioning of Fe and Mg between melt and all the coexisting phases, and the exchange K_D's for Fe and Mg are calculated from the experimental data set. The value for K_D^{Fe-Mg} for olivine is known to vary with pressure and melt composition (Ulmer 1989; Toplis 2005). We set the K_D^{Fe-Mg} values for clinopyroxene, orthopyroxene and garnet to 1.06, 0.97 and 1.5 times the K_D^{Fe-Mg} value for olivine melt as discussed by Kinzler and Grove (1992b) and Kinzler (1997), allowing the compositional variations in K_D^{Fe-Mg} to be applied to all phases.

In order to compare the garnet lherzolite model presented in this study to the model of Longhi (2002), we performed melting calculation at 10 and 1 % wt. melting of the Hart and Zindler (1986) primitive mantle composition and the depleted Hart and Zindler mantle composition (Kinzler and Grove 1992b) at a pressure of 3 GPa (Table 5). In general, the compositions compare well with one another. Our model calculations have FeO systematically higher than Longhi (2002) by 3–7 % relative (or <2 wt%). The FeO in the predictions by Longhi (2002) appear to be closer to the abundances expected in the spinel stability field. The higher values predicted by our model are more consistent with our input data (Walter 1998) for the lherzolite melting. There are also large differences in the calculated Na_2O abundances between the two models (30–50 %). The Longhi (2002) melts have significantly higher Na_2O than the melts predicted by the model presented here. The causes of this difference are not clear. One important aspect of our model is that it calculates a partition coefficient for Na_2O in cpx and opx that is positively correlated with pressure, leading to less Na_2O in high-pressure garnet lherzolite melts. Longhi (2002) also states that he calculates pressure-dependent partition coefficients, so this may not be an explanation for the difference.

Another test of our melting model is to see how well it recovers a melting experiment of a natural peridotite. Two of the input experiments used in our model expressions that predict the composition of garnet lherzolite MSPs are melts of lherzolite bulk composition (Walter 1998, expts. 40.07 and 60.05). Table 5 compares experimental melt composition 40.07 with the liquid composition predicted by our melting model. This liquid composition was predicted by using the Walter (1998) Kettle River lherzolite composition as input along with the pressure of the experiment and the Walter (1998) experimental olivine/melt K_D^{Fe-Mg} of 0.36. The predicted liquid composition compares favorably for all elements with the exception of the predicted abundance of Na_2O and TiO_2. This may be a consequence of the model partition coefficients that are fit to a larger data set that includes studies with lower partition coefficients than those reported by Walter (1998). The temperature of experiment 40.07 is also recovered by the model to within 12 °C (Table 5).

In its current implementation, melting styles can be specified as either batch or polybaric near-fractional adiabatic decompression melting. Melt production rates for polybaric melting can be varied depending on preference

Table 5 Comparison of garnet lherzolite melting model of Longhi and test of model

	Primitive H&Z 10 and 1 % melts				Depleted H&Z 10 and 1 % melts			
	10 %[a]	L '02	1 %	L '02	10 %	L '02	1 %	L '02
SiO_2	45.0	46.2	44.2	45.6	45.3	46.0	44.4	44.9
TiO_2	1.14	0.98	2.06	1.43	1.05	0.97	2.07	1.61
Al_2O_3	13.1	13.0	15.8	15.1	12.8	12.8	13.5	14.3
Cr_2O_3	0.18	0.32	0.13	0.22	0.18	0.34	0.15	0.29
FeO	10.5	9.60	9.32	9.60	10.3	9.70	10.4	10.1
MgO	17.9	18.1	14.8	15.3	18.5	18.5	17.4	17.2
CaO	10.8	9.76	9.93	6.91	10.9	10.1	10.3	8.34
Na_2O	1.02	1.57	1.41	2.68	0.91	1.32	1.29	1.96
K_2O	0.29	0.28	2.27	2.13	0.07	0.07	0.59	0.54

	40.07[b]	Model[c]
SiO_2	45.5	45.4
TiO_2	1.27	0.88
Al_2O_3	10.3	11.1
Cr_2O_3	0.25	0.16
FeO	10.7	11.1
MgO	19.9	20.1
CaO	9.31	10.1
Na_2O	1.08	0.64
K_2O	0.7	0.65
T (°C)	1,610	1,622

Model calculation at 3 GPa and 10 and 1 % melting from this study and Longhi (2002)

[a] Melts of Hart and Zindler primitive (Hart and Zindler 1986) and depleted (Kinzler and Grove 1992b) mantle compositions

[b] 40.07 shows the composition and temperature of a Lherzolite melt from Walter (1998) at 4 GPa and 13 wt% melting

[c] Forward model of melting using the Walter (1998) lherzolite composition and 13 % melting at 4 GPa. Temperature is that predicted by the model

for the heat of fusion. Asimow et al. (1997) calculate isentropic melt production rates for lherzolite and find them to vary with melt fraction, a feature that can be implemented in this model. Effects of phase transitions from garnet to spinel facies and spinel to plagioclase facies can also influence melting rate (Asimow et al. 1995), and these can be incorporated in the model. It is difficult to directly compare our model to the PRIMELT.XLS model of Herzberg and Asimow (2008), because they implement a model that does not explicitly vary mantle lherzolite bulk composition. However, we would anticipate that our model of garnet lherzolite melting would, at the very least, be an improvement for predicting melts of metasomatized mantle lherzolite (compositions for which the PRIMELT.XLS is not calibrated).

Conclusions

We develop a model for predicting the compositions of melts in equilibrium with garnet lherzolite under anhydrous conditions. When combined with the plagioclase and spinel lherzolite melting models of Till et al. (2012), primary magmas from lherzolite melting can now be quantitatively predicted from 0.1 MPa to 6 GPa. We demonstrate how the predicted lherzolite melt compositions can be distinguished from melts of pyroxenite source materials and melts of carbonated lherzolite based on major element compositional characteristics.

Acknowledgments The paper is dedicated to the memory of a great igneous petrologist, Ian Carmichael. Ian was like a father to many of us. He was always there to provide encouragement, support and criticism. Often all three of these were administered with equal enthusiasm. This work was first presented at a career celebration for Ian held at Camp Davis field station, Wyoming, August 12–16, 2005. Support for this work was provided through the National Science Foundation from grants EAR-0507486, EAR-0538179 and EAR-1118598. The authors gratefully acknowledge constructive comments of two anonymous reviewers and Tom Sisson, who suggested that we look at the melting conditions of the common and voluminous alkali basalts and tholeiites present at Hawaii.

References

Armstrong JT (1995) CITZAF—a package of correction programs for the quantitative electron microbeam X-ray analysis of thick polished materials, thin-films, and particles. Microbeam Anal 4:177–200

Asimow PD, Hirschmann MM, Ghiorso MS, Ohara MJ, Stolper EM (1995) The effect of pressure-induced solid–solid phase-transitions on decompression melting of the mantle. Geochim Cosmochim Acta 59(21):4489–4506

Asimow PD, Hirschmann MM, Stolper E (1997) An analysis of variations in isentropic melt productivity. Philos Trans R Soc Lond Ser A 355:255–281

Baker MB, Stolper EM (1994) Determining the composition of high-pressure mantle melts using diamond aggregates. Geochim Cosmochim Acta 58(13):2811–2827

Barr JA, Grove TL (2013) Experimental petrology of the Apollo 15 group A green glasses: melting primordial lunar mantle and magma ocean cumulate assimilation. Geochim Cosmochim Acta. doi:10.1016/j.gca.2012.12.035

Boyd FR, England JL (1960) Apparatus for phase equilibrium studies at pressures up to 50 kilobars and temperatures up to 1750 °C. J Geophys Res 65:741–748

Brey G, Green DH (1975) Role of CO_2 in genesis of olivine melilite. Contrib Mineral Petrol 49(2):93–103. doi:10.1007/bf00373853

Clague DA (1987) Hawaiian alkaline volcanism. In: Fitton JG, Upton BGJ (eds) Alkaline igneous rocks. Geol Soc Spec Pub 30:227–252

Clague DA, Moore JG, Dixon JE, Freisen WB (1995) Petrology of submarine lavas from Kilauea's Puna Ridge, Hawaii. J Petrol 36(2):299–349

Clague DA, Davis AL, Bischoff JL, Dixon JE, Geyer R (2000) Lava bubble-wall fragments formed by submarine hydrovolcanic explosions on Loihi seamount and Kilauea volcano. Bull Volcanol 61:437–449

Coombs ML, Sisson TW, Lipman PL (2004) Major element, sulfur, and chlorine concentrations of glasses from the submarine flank of Kilauea volcano, Hawaii, collected during the 1998–2002 Japan Marine Science and Technology Center (JAMSTEC) cruises. U.S. Geological Survey Open File Report: OF 2004–1378, p 7. http://pubs.usgs.gov/of/2004/1378

Dasgupta R, Hirschmann MM (2006) Melting in the Earth's deep upper mantle caused by carbon dioxide. Nature 440(7084): 659–662. doi:10.1038/nature04612

Dasgupta R, Hirschmann MM (2007) Effect of variable carbonate concentration on the solidus of mantle peridotite. Am Mineral 92:370–379

Dasgupta R, Hirschmann MM, Smith ND (2007) Partial melting experiments of peridotite CO_2 at 3 GPa and genesis of alkalic ocean island basalts. J Petrol 48(11):2093–2124. doi:10.1093/petrology/egm053

Ding L, Kapp P, Zhong DL, Deng WM (2003) Cenozoic volcanism in Tibet: evidence for a transition from oceanic to continental subduction. J Petrol 44(10):1833–1865

Eggins SM (1992) Petrogenesis of Hawaiian tholeiites: 2. Aspects of dynamic melt segregation. Contrib Mineral Petrol 110:398–410

Eggler DH (1978) Effect of CO_2 upon partial melting of peridotite in system Na_2O–CaO–Al_2O_3–MgO–SiO_2–CO_2 to 35 kb, with an analysis of melting in a peridotite-H_2O–CO_2 system. Am J Sci 278(3):305–343

Frey FA, Wise WS, Garcia MO, West H, Kwon ST, Kennedy A (1990) Evolution of Mauna Kea Volcano, Hawaii: petrologic and geochemical constraints on postshield volcanism. J Geophys Res 95:1271–1300

Gaetani GA, Grove TL (1998) The influence of water on melting of mantle peridotite. Contrib Mineral Petrol 131(4):323–346

Garcia MO, Muenow DW, Aggrey KE, O'Neill JR (1989) Major element, volatile, and stable isotope geochemistry of Hawaiian submarine tholeiitic glasses. J Geophys Res 94(B8):10525–10538

Garcia MO, Foss DJO, West HB, Mahoney JJ (1995) Geochemical and isotopic evolution of Loihi volcano, Hawaii. J Petrol 36:1647–1674

Grove TL, Bence AE (1977) Experimental study of pyroxene-liquid interaction in quartz-normative basalt 15597. Proc Lunar Sci Conf 8:1549–1579

Gudfinnsson GH, Presnall DC (1996) Melting relations of model lherzolite in the system CaO–MgO–Al_2O_3–SiO_2 at 2.4-3.4 GPa and the generation of komatiites. J Geophys Res 101(B12): 27701–27709. doi:10.1029/96jb02462

Gudfinnsson GH, Presnall DC (2005) Continuous gradations among primary carbonatitic, kimberlitic, melilititic, basaltic, picritic and komatiitic melts in equilibrium with garnet lherzolite at 3–8 GPa. J Petrol 46(7):1645–1659

Guo ZF, Wilson M, Liu JQ, Mao Q (2006) Post-collisional, potassic and ultrapotassic magmatism of the northern Tibetan Plateau: constraints on characteristics of the mantle source, geodynamic setting and uplift mechanisms. J Petrol 47(6):1177–1220

Hart SR, Zindler A (1986) In search of a bulk-earth composition. Chem Geol 57(3–4):247–267

Hays JF (1967) Lime-alumina-silica. In: Carnegie Institution of Washington Year Book, vol 65. Carnegie Institution of Washington, Washington, DC, pp 234–239

Herzberg C, Asimow PD (2008) Petrology of some oceanic island basalts: PRIMELTS2.XLS software program for primary magma calculation. Geochem Geophys Geosyst 9:art. no.-Q09001

Hesse M, Grove TL (2003) Absarokites from the western Mexican Volcanic Belt: constraints on mantle wedge conditions. Contrib Mineral Petrol 146:10–27

Hirose K (1997) Partial melt compositions of carbonated peridotite at 3 GPa and role of CO_2 in alkali-basalt magma generation. Geophys Res L 24(22):2837–2840. doi:10.1029/97gl02956

Hirschmann MM, Kogiso T, Baker MB, Stolper EM (2003) Alkalic magmas generated by partial melting of garnet pyroxenite. Geology 31(6):481–484

Hofmann AW, Feigenson MD, Raczek I (1984) Case studies on the origin of basalt: III. Petrogenesis of the Mauna Ulu erup-tion, Kilauea, 1969–1971. Contrib Mineral Petrol 88:24–35

Holbig ES, Grove TL (2008) Mantle melting beneath the Tibetan Plateau: experimental constraints on the generation of ultra-potassic lavas from Qiangtang, Tibet. J Geophys Res 113(B04210). doi:10.1029/2007JB005149

Johannes W, Chipman DW, Hays JF, Bell PM, Mao HK, Newton RC, Boettcher AL, Seifert F (1971) An interlaboratory comparison of piston-cylinder pressure calibration using the albite-breakdown reaction. Contrib Mineral Petrol 32:24–38

Kinzler RJ (1997) Melting of mantle peridotite at pressures approaching the spinel to garnet transition: application to mid-ocean ridge basalt petrogenesis. J Geophys Res 102(B1): 853–874

Kinzler RJ, Grove TL (1992) Primary magmas of midocean ridge basalts 1. Experiments and methods. J Geophys Res 97(B5): 6885–6906

Kinzler RJ, Grove TL (1992) Primary magmas of midocean ridge basalts 2. Applications. J Geophys Res 97(B5):6907–6926

Kinzler RJ, Grove TL (1993) Corrections and further discussion of the primary magmas of mid-ocean ridge basalts, 1 and 2. J Geophys Res 98(B12):22339–22347

Kinzler RJ, Grove T (1999) Origin of depleted cratonic harzburgites by deep fractional melt extraction and shallow olivine cumulate infusion. In: Gurney JJ (ed) Proceedings of the 7th international kimberlite conference, pp 437–443

Klemme S, O'Neill HSC (2000) The near-solidus transition from garnet lherzolite to spinel lherzolite. Contrib Mineral Petrol 138(3):237–248. doi:10.1007/s004100050560

Kogiso T, Hirose K, Takahashi E (1998) Melting experiments on homogeneous mixtures of peridotite and basalt: application to the genesis of ocean island basalts. Earth Planet Sci Lett 162(1–4):45–61. doi:10.1016/s0012-821x(98)00156-3

Kogiso T, Hirschmann MM, Frost DJ (2003) High-pressure partial melting of garnet pyroxenite: possible mafic lithologies in the source of ocean island basalts. Earth Planet Sci Lett 216(4):603–617. doi:10.1016/s0012-821x(03)00538-7

Kogiso T, Hirschmann MM, Pertermann M (2004) High-pressure partial melting of mafic lithologies in the mantle. J Petrol 45(12):2407–2422. doi:10.1093/petrology/egh057

Krawczynski MJ, Olive JL (2011) A new fitting algorithm for petrologic mass-balance problems. Abstract V53B-2613, presented at 2011 Fall Meeting, AGU, San Francisco, Calif, 5–9 Dec

Kushiro I (1975) Nature of silicate melt and its significance in magma genesis—regularities in shift of liquidus boundaries involving olivine, pyroxene and silica minerals. Am J Sci 275(4):411–431

Kushiro I (1996) Partial melting of a fertile mantle peridotite at high pressures: an experimental study using aggregates of diamond. In: Basu A, Hart SR (eds) Earth processes: reading the isotopic code AGU monograph, vol 95. American Geophysical Union, Washington, DC, pp 109–122

Longhi J (1995) Liquidus equilibria of some primary lunar and terrestrial melts in the garnet stability. Geochim Cosmochim Acta 59(11):2375–2386

Longhi J (2002) Some phase equilibrium systematics of lherzolite melting: I. Geochem Geophys Geosyst 3:art. no.-1020

Longhi J (2005) Temporal stability and pressure calibration of barium carbonate and talc/pyrex pressure media in a piston-cylinder apparatus. Am Mineral 90:206–218

MacDonald GA, Katsura T (1964) Chemical composition of Hawaiian lavas. J Petrol 5:82–133

MacGregor I (1965) Stability fields of spinel and garnet peridotites in the synthetic system $CaO–MgO–Al_2O_3–SiO_2$. Carnegie Inst Wash Year Book 64:126–134

Médard E, McCammon CA, Barr JA, Grove TL (2008) Oxygen fugacity, temperature reproducibility, and H_2O contents of nominally anhydrous piston-cylinder experiments using graphite capsules. Am Mineral 93:1838–1844

Moore JG, Clague DA (1987) Coastal lava flows from Mauna Loa and Hualalai, Kona, Hawaii. Bull Volcanol 57:752–764

Moore JG, Clague DA, Normark WA (1982) Diverse basalt types from Loihi seamount, Hawaii. Geology 10:88–92

Moore JG, Fornari DJ, Clague DA (1985) Basalts from the 1977 submarine eruption of Mauna Loa, Hawaii: new data on the variation of palagonitization rate with temperature. U S Geol Survey Bull 1663:1–11

Naka J, Kanamatsu T, Lipman PW, Sisson TW, Tsuboyama N, Morgan JK, Smith JR, Ui T (2002) Deep-sea volcaniclastic sedimentation around the southern flank of Hawaii. In: Takahashi E, Lipman PW, Garcia MO, Naka J, Aramaki S (eds) Hawaiian volcanoes: deep underwater perspectives. Amer Geophys Union Geophys Monogr 128:29–50

Nomade S, Renne PR, Mo XX, Zhao ZD, Zhou S (2004) Miocene volcanism in the Lhasa block, Tibet: spatial trends and geodynamic implications. Earth Planet Sci Lett 221(1–4):227–243

O'Neill HSC (1981) The transitions between spinel lherzolite and garnet lherzolite, and its use as a geobarometer. Contrib Mineral Petrol 77(2):185–194. doi:10.1007/bf00636522

O'Hara MJ, Richardson SW, Wilson G (1971) Garnet peridotite stability and occurrence in crust and mantle. Contrib Mineral Petrol 32:48–68

Pertermann M, Hirschmann MM, Hametner K, Gunther D, Schmidt MW (2004) Experimental determination of trace element partitioning between garnet and silica-rich liquid during anhydrous partial melting of MORB-like eclogite. Geochem Geophys Geosyst 5. doi:10.1029/2003gc000638

Presnall DC, Dixon JR, O'Donnell TH, Dixon SA (1979) Generation of mid-ocean ridge tholeiites. J Petrol 20:3–35

Sisson TW, Lipman PW, Naka J (2002) Submarine alkalic through tholeiitic shield-stage development of Kilauea volcano, Hawaii. In: Takahashi E, Lipman PW, Garcia MO, Naka J, Aramaki S (eds) Hawaiian volcanoes: deep underwater perspectives. Amer Geophys Union Geophys Monogr 128:193–219

Sisson TW, Kimura JI, Coombs ML (2009) Basanite-nephelinite suite from early Kilauea: carbonated melts of phlogopite-garnet

peridotite at Hawaii's leading magmatic edge. Contrib Mineral Petrol 158(6):803–829. doi:10.1007/s00410-009-0411-8

Sobolev AV, Hofmann AW, Sobolev SV, Nikogosian IK (2005) An olivine-free mantle source for Hawaiian shield lavas. Nature 434(7033):590–597

Stolper E, Sherman S Garcia M, Baker M, Seaman S (2004) Glass in the submarine section of the HSDP2 drill core, Hilo, Hawaii. Geochem Geophys Geosyst 5:Q07G15. doi:10.1029/2003gc000553

Takahahshi E, Nakajima K, Wright TL (1998) Origin of the Columbia River basalts: melting model of a heterogeneous plume head. Earth Planet Sci Lett 162(1–4):63–80. doi:10.1016/s0012-821x(98)00157-5

Takahashi E (1986) Melting of a dry peridotite KLB-1 up to 14 GPa—implications on the origin of peridotitic upper mantle. J Geophys Res 91(B9):9367–9382

Thibault Y, Edgar AD, Lloyd FE (1992) Experimental investigation of melts from a carbonated phlogopite lherzolite—implications for metasomatism in the continental lithospheric mantle. Am Mineral 77(7–8):784–794

Till CB, Grove TL, Krawczynski MJ (2012) A melting model for variably depleted and enriched lherzolite in the plagioclase and spinel stability fields. J Geophys Res 117. doi:10.1029/2011jb009044

Toplis MJ (2005) The thermodynamics of iron and magnesium partitioning between olivine and liquid: criteria for assessing and predicting equilibrium in natural and experimental systems. Contrib Mineral Petrol 149:22–39

Tormey DR, Grove TL, Bryan WB (1987) Experimental petrology of normal MORB near the Kane fracture zone: 22–25 N, mid-Atlantic ridge. Contrib Mineral Petrol 96:121–139

Ulmer P (1989) The dependence of the Fe2+-Mg cation-partitioning between olivine and basaltic liquid on pressure, temperature and composition; an experimental study to 30 kbars. Contrib Mineral Petrol 101(3):261–273

Wagner TP, Grove TL (1998) Melt/harzburgite reaction in the petrogenesis of tholeiitic magma from Liauea volcano, Hawaii. Contrib Mineral Petrol 131(1):1–12

Walker D, Agee CB (1988) Ureilite compaction. Meteoritics 23(1):81–91

Walter MJ (1998) Melting of garnet peridotite and the origin of komatiite and depleted lithosphere. J Petrol 39(1):29–60

Walter MJ, Presnall DC (1994) Melting behavior of simplified lherzolite in the system CaO–MgO–Al_2O_3–SiO_2–Na_2O from 7 to 35 kbar. J Petrol 35(2):329–359

Williams HM, Turner SP, Pearce JA, Kelley SP, Harris NBW (2004) Nature of the source regions for post-collisional, potassic magmatism in southern and northern Tibet from geochemical variations and inverse trace element modeling. J Petrol 45(3):555–607

Wyllie PJ, Huang WL (1976) Carbonation and melting reactions in system CaO–MgO–SiO_2–CO_2 at mantle pressures with geophysical and petrological applications. Contrib Mineral Petrol 54(2):79–107. doi:10.1007/bf00372117

Yang HJ, Kinzler RJ, Grove TL (1996) Experiments and models of anhydrous, basaltic olivine-plagioclase-augite saturated melts from 0.001 to 10 kbar. Contrib Mineral Petrol 124:1–18